

A Non-ergodic Effective Amplitude Ground-Motion Model for California

Grigorios Lavrentiadis^{*1}, Norman A. Abrahamson^{†1} and Nicolas M. Kuehn^{‡2}

¹Department of Civil Engineering, University of California, Berkeley

²B. John Garrick Institute for the Risk Sciences, University of California, Los Angeles

June 25, 2021

Abstract

A new non-ergodic ground-motion model (GMM) for effective amplitude spectral (*EAS*) values for California is presented in this study. *EAS*, which is defined in Goulet et al. (2018), is a smoothed rotation-independent Fourier amplitude spectrum of the two horizontal components of an acceleration time history. The main motivation for developing a non-ergodic *EAS* GMM, rather than a spectral acceleration GMM, is that the scaling of *EAS* does not depend on spectral shape, and therefore, the more frequent small magnitude events can be used in the estimation of the non-ergodic terms.

The model is developed using the California subset of the NGAWest2 dataset Ancheta et al. (2013). The Bayless and Abrahamson (2019b) (BA18) ergodic *EAS* GMM was used as backbone to constrain the average source, path, and site scaling. The non-ergodic GMM is formulated as a Bayesian hierarchical model: the non-ergodic source and site terms are modeled as spatially varying coefficients following the approach of Landwehr et al. (2016), and the non-ergodic path effects are captured by the cell-specific anelastic attenuation following the approach of Dawood and Rodriguez-Marek (2013). Close to stations and past events, the mean values of the non-ergodic terms deviate from zero to capture the systematic effects and their epistemic uncertainty is small. In areas with sparse data, the epistemic uncertainty of the non-ergodic terms is large, as the systematic effects cannot be determined.

The non-ergodic total aleatory standard deviation is approximately 30 to 40% smaller than the total aleatory standard deviation of BA18. This reduction in the aleatory variability has a significant impact on hazard calculations at large return periods. The epistemic uncertainty of the ground motion predictions is small in areas close to stations and past events.

1 Introduction

Probabilistic seismic hazard analysis (PSHA) estimates the annual rate of exceeding a ground-motion parameter at a site of interest. It typically breaks the problem in two parts: the seismic

^{*}glavrent@berkeley.edu

[†]abrahamson@berkeley.edu

[‡]kuehn@g.ucla.edu

source characterization and the ground-motion model (GMM). The first part defines the rate, the magnitude distribution, and the location distribution of earthquakes in a region, and the second part, which is the focus of this study, provides the probability of exceeding the ground-motion for a specific earthquake scenario. Most GMM are derived empirically using strong-motion datasets and define the distribution of the ground-motion parameter as a function of source, path, and site parameters such as magnitude (M), closest rupture distance (R_{rup}) and time-averaged shear-wave velocity in the top 30m (V_{S30}). Traditionally, due to the scarcity of regional data, GMM were developed under the ergodic approach which assumes the statistical properties of the ground-motion parameter do not change in space (Anderson and Brune, 1999). These ergodic models tend to have large aleatory variability as they treat some of the systematic effects for a specific site/source location as random variability that can occur anywhere. Examples of models that have been developed under this approach are the NGA-West GMMs for California (Abrahamson et al., 2008), and the European GMMs derived from the RESORCE database (Douglas et al., 2014); however, as more data are collected, the ergodic assumption can be relaxed, and repeatable effects related to the source, path and site can be properly modeled, which leads to a decrease in the aleatory variability. This reduction has a large impact on the hazard at large return periods because, the ground-motion aleatory variability controls the slope of the hazard curves which has a large influence on the hazard at large return periods. Al Atik et al. (2010) describes how the aleatory variability of an ergodic model can be separated into epistemic uncertainty related to the systematic source, path, and site terms, and the reduced aleatory variability of a non-ergodic GMM. The epistemic uncertainty refers to the range by which the non-ergodic terms vary in areas with no available data to constrain them. In areas with data from past earthquakes, the non-ergodic terms can be estimated, and their epistemic uncertainty can be reduced.

The first step in this new paradigm was to create a regional GMM or a global GMM with some regionalized terms. Regional GMMs are developed with smaller regional data-sets, for instance Akkar and Çağnan (2010) for Turkey, Bindi et al. (2011) for Italy, Bragato and Slejko (2005) for Eastern Alps, and Danciu and Tselentis (2007) for Greece. These models have smaller aleatory variability than global ergodic GMMs, but they suffer from weaker constraints on the scaling due to the smaller size of the regressed data sets. Global GMMs with regionalized terms are developed with large global datasets, the same way ergodic GMM are developed but with the difference that some of the scaling terms are estimated separately for each region. The NGAWest2 GMM (Bozorgnia et al., 2014) followed this approach. For example, in Abrahamson et al. (2014), both the V_{S30} and anelastic attenuation scaling terms were regionalized: they have a different set of coefficients for California, China, Japan, and Taiwan.

Partially non-ergodic GMMs that only capture the systematic site effects, known as single station GMMs, lead to an approximately 30% reduction in the aleatory variance compared to an ergodic GMM (Coppersmith et al., 2014; Bommer et al., 2015; Tromans et al., 2019). Similarly, other researchers have developed partially non-ergodic GMMs that capture repeatable effects related to the source (Yagoda-Biran et al., 2015), path (Dawood and Rodriguez-Marek, 2013; Kuehn et al., 2019), and single source/single site (Hiemer et al., 2011). Fully non-ergodic GMMs include non-ergodic terms to capture simultaneously all the aforementioned systematic effects (source, path, and site); these type of models have 60 to 70% smaller aleatory variance than ergodic GMMs (Lin et al., 2011; Landwehr et al., 2016; Abrahamson et al., 2019).

The model presented in this study is a fully non-ergodic GMM that captures the systematic effects of the source, site, and anelastic attenuation from the path. It is developed as spatially varying coefficient model (VCM), following the methodology used in Bussas et al. (2017) and Landwehr et al. (2016). The non-ergodic anelastic attenuation is modeled with the cell-specific

anelastic attenuation similar to Dawood and Rodriguez-Marek (2013) and Abrahamson et al. (2019). VCMs impose a spatial correlation on the coefficients, so that they vary continuously from location to location; alternative methods to impose the spatial correlation are: splines, and neural networks. In the cell-specific anelastic attenuation approach, the domain of interest is broken into cells which all have their own attenuation coefficient. The attenuation along a path from a source to site is equal to the sum of attenuation of the cells that it traverses.

One distinction of the current model from other non-ergodic GMMs is that it is developed for effective amplitude spectral (*EAS*) values instead of response spectral accelerations (*PSA*). This is done because it is easier for the *EAS* non-ergodic effects estimated from small events to be transferred to large magnitude earthquakes than for the *PSA* non-ergodic effects. The response of a small-period single-degree-of-freedom oscillator (SDOF) is affected by the entire frequency content of the ground motion, as amplitude of the short-period ground motion is too small control the SDOF response. This makes the short-period *PSA* sensitive to the ground motion at frequencies near the peak in the *FAS* due to their higher amplitudes. The frequency content and period of the *FAS* peak change with magnitude: as the magnitude of an earthquake increases, the period of the peak also increases, making the scaling of the small-period *PSA* magnitude dependent. It is this magnitude dependence of the *PSA* scaling that makes the short-period non-ergodic terms of the small magnitudes not transferable to large magnitude events without modification. A detailed discussion of the scaling of *FAS* and *PSA* is given by ?.

As an example, the response spectrum of an *M3* event has its peak at $T = 0.1sec$, whereas the *M7* response spectrum from has its peak at $T = 0.3sec$; a sketch illustrating their different spectral shapes is provided in the electronic supplement. Due to this spectral shape difference, the *PGA* scaling will be consistent with the scaling of the *PSA*($T = 0.1sec$) at small magnitudes and with the scaling of the *PSA*($T = 0.3sec$) at large magnitudes. For example, to properly capture the magnitude dependence in a *PSA* GMM, the V_{S30} coefficient for *PGA* would be close to the V_{S30} coefficient for $T = 0.1sec$ at small magnitudes, and it should gradually shift towards the V_{S30} coefficient for $T = 0.3sec$ as magnitude increases. This is consistent with Stafford et al. (2017), who showed that the linear site amplification factors are magnitude and distance dependent.

The *EAS* is defined in Goulet et al. (2018) as the smoothed power-averaged Fourier amplitude spectrum (*FAS*) of the two horizontal components. The *EAS* does not suffer from the same problem as *PSA* because the Fourier transform is a linear operation, and the scaling coefficients and non-ergodic terms estimated from small magnitude earthquakes can be applied directly to large events for linear source, path, and site effects. To ensure that the proposed model extrapolates reasonably to scenarios outside the range of events in the regression data set, we use the Bayless and Abrahamson (2019b) ergodic *EAS* GMM (BA18) as a backbone model; we selected BA18 because it was developed on a large global data-set, and it includes seismological constraints to avoid oversaturation at short distances and large magnitudes. The non-ergodic terms and cell-specific anelastic attenuation coefficients were estimated with the total residuals of BA18 from the NGAWest2 California subset.

Lastly, one common comment regarding the usage of an *EAS* GMM is that, in most seismic design methods, the intensity of the ground-motion shaking is specified in terms of *PSA* and not *EAS*. We can use an *EAS* GMM and Random Vibration Theory (RVT) to compute the equivalent *PSA*. RVT uses *FAS* and the duration of an SDOF oscillator response to a ground motion to compute the root-mean-square amplitude of the response (x_{rms}), based on Parseval's theorem. The spectral acceleration, which is the peak response of the SDOF, is estimated by the product of x_{rms} and the peak factor. Boore (1983) used RVT with *FAS* from seismological theory to calculate the equivalent *PSA*, and Bora et al. (2015, 2019) derived a duration model

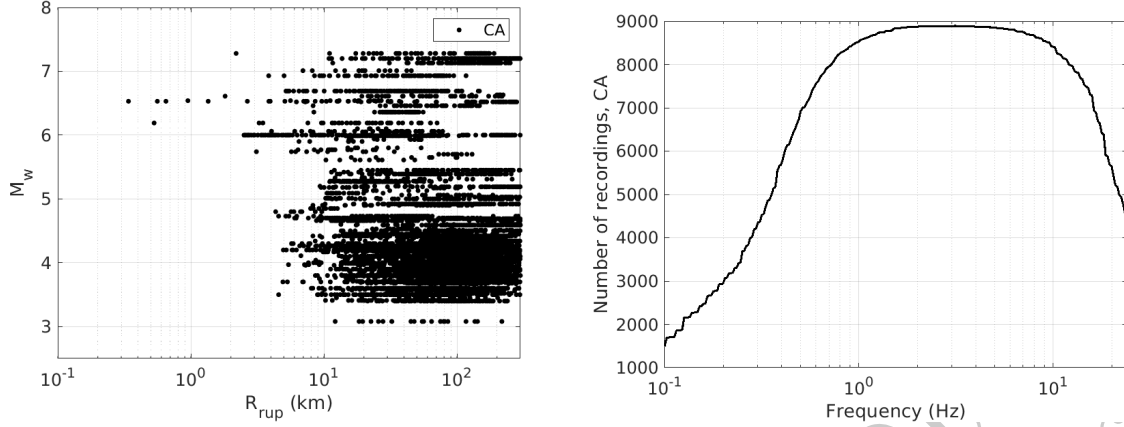


Figure 1: Selected data from the NGAWest2 database. The left figure shows Magnitude - Distance distribution of the subset used in the regression analysis. The right figure the number of recordings per frequency used in the regression analysis.

which, when used with a Brune (1970, 1971) omega-squared FAS model, gives predictions that are consistent with the NGAWest2 data set. Converting the non-ergodic *EAS* GMM into an equivalent *PSA* GMM is not in the scope of this paper; it is covered in the second part of this study. In this approach, the median estimate of the non-ergodic *PSA* GMM is based on the median estimate of the *EAS* GMM and RVT, while the non-ergodic aleatory variability is estimated empirically using the ground-motion observations.

2 Ground-Motion Data

The NGAWest2 data-base (Ancheta et al., 2014) includes more than 21000 recordings covering a magnitude range from 3 to 7.9 and a closest distance range (R_{rup}) from 0.05 to 1500 km. For this study, a subset of this data-base was used which included the earthquakes and stations located in California, western Nevada, and northern Mexico. The recordings that were identified as questionable in Abrahamson et al. (2014) were not used in the regressions. The final data-set contains 8916 recordings from 188 earthquakes recorded at 1497 stations. Figure 1 shows the magnitude-distance distribution of the data and the number of recordings per frequency. The earthquake magnitudes in the selected data range from 3.1 to 7.3 and the distances range from 0.1 to 300 km. The usable frequency range of the majority of the recordings spans from 1 and 10 Hz.

Figure 2 shows the spatial distribution of the data: most of the stations are located in Los Angeles, Bay Area, and San Diego metropolitan areas, whereas in less populated areas, such as northern-eastern California the spatial density of the stations is lower. This difference in the density of stations has a large impact on the distribution of epistemic uncertainty of the systematic site effects: the epistemic uncertainty is higher in areas with lower station density making a case for expanding the strong-motion networks in these regions near critical infrastructure. In this study, the location of the earthquakes and stations is defined in kilometers in UTM coordinates; the longitude/latitude coordinates were transformed to UTM coordinates using the WGS84 reference ellipsoid and 11S UTM zone.

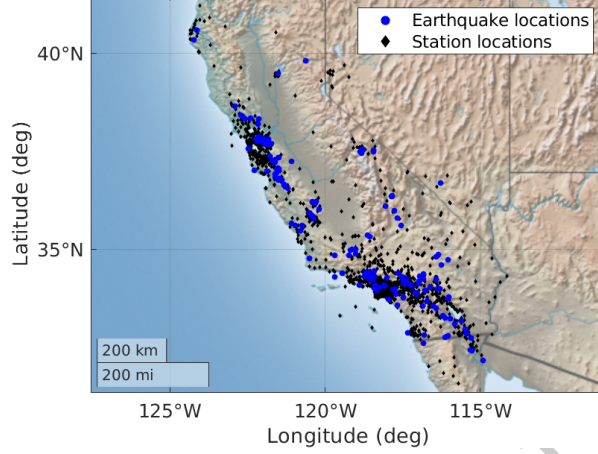


Figure 2: Spatial distribution for earthquakes and stations used in this study.

3 Non-ergodic Model Development

Rather than developing the non-ergodic GMM from scratch, the Bayless and Abrahamson (2019b) (BA18) ergodic EAS GMM was used as a backbone model to describe the average ground-motion scaling. The main reasons for that decision were that: i) the local data may non be adequate to estimate the scaling of complex terms, and ii) the adoption of the constraints built into BA18 ensures that it extrapolates properly outside the range of data.

3.1 Functional Form

Typically, a GMM (Equation (1)) is composed of the median model (y_{med}) and the aleatory variability. The median model describes the average scaling of a ground-motion parameter with magnitude, distance, site conditions, etc. The aleatory variability describes the misfit between a ground-motion observation and y_{med} which is related to the true or apparent (due to simplified modeling) stochastic behavior of the source, site, and path. It is typically expressed as the sum of the between-event (δB_e) and within-event ($\delta W_{e,s}$) terms. $\delta B_{e,s}$ describes average shift of the ground motion for an earthquake, e , from y_{med} , and $\delta W_{e,s}$ describes the variability of the ground motion at site, s from the median ground motion of that earthquake.

$$\ln(EAS) = y_{med} + \delta B_e + \delta W_{e,s} \quad (1)$$

The median EAS model of Bayless and Abrahamson (2019b) is formulated as:

$$y_{med} = f_M + f_R + f_S + f_{ztor} + f_{NM} + f_{Z1} \quad (2)$$

where f_M is the magnitude scaling, f_R is the path scaling, f_S is the site scaling, f_{ztor} is the top of rupture scaling, f_{NM} is the normal-fault scaling, and f_{Z1} is the basin thickness scaling. The f_M , f_R and f_S terms were modified to include the additional non-ergodic terms, whereas f_{ztor} , f_{NM} and f_{Z1} were kept fixed. The different terms and coefficients are described in detail in Bayless and Abrahamson (2019b) and Chiou and Youngs (2014).

3.1.1 Magnitude Scaling

The f_M in the non-ergodic model is:

$$f_M = c_1 + c_2(M - 6) + \frac{c_2 - c_3}{c_n} \ln(1 + e^{c_n(c_M - M)}) + \delta c_0 + \delta c_{0,e} + \delta c_{1,e}(\vec{x}_e) \quad (3)$$

in which c_1 is the intercept of the model, c_2 controls the magnitude scaling for large magnitudes where the corner frequency is smaller than the frequency of interest, $(c_2 - c_3)/c_n$ describes the magnitude scaling at small magnitudes, where the corner-frequency is larger than the frequency of interest, c_n controls the width of the transition zone between small and large magnitude earthquakes, and c_M is the magnitude at the center of the transition zone. A sketch of the magnitude scaling is provided in the electronic supplement.

The additional coefficients in the non-ergodic model are δc_0 , $\delta c_{0,e}$, and $\delta c_{1,e}$. δc_0 is added to allow a small constant shift in the non-ergodic model due the difference in the weighting of residuals between the ergodic and non-ergodic GMMs. $\delta c_{1,e}$ is a function of the earthquake coordinates, \vec{x}_e , and is intended to capture repeatable non-ergodic effects related to the source location. For instance, regions with a higher than average median stress drop will have higher than average median ground-motions resulting in a positive $\delta c_{1,e}$. $\delta c_{0,e}$ is a regional term that corrects a potential bias in the magnitude estimation of small earthquakes between northern and southern California. $\delta c_{0,e}$ is applied to earthquakes less than magnitude 5 and frequencies less than $5Hz$. The vertices which define the polygons for the northern and southern CA subregions are summarized in Table 1, the border between northern and southern CA corresponds approximately to the boundary between the Northern California Seismic Network (NCSN) and Southern California Seismic Network (SCSN).

The $\delta c_{0,e}$ term addresses potential inconsistencies in the reported magnitudes of small earthquakes between northern and southern CA because the NCSN/SCSN boundary was also used in the NGAWest2 dataset Ancheta et al. (2013) for the selecting the catalog to use for the source parameters (magnitude, hypocenter location, etc.) for small-to-moderate (less than $M 5$) earthquakes. If a small earthquake was located north of the boundary, the NCSN catalog was used for the source parameters, whereas if a small earthquake was located south of the boundary, the SCSN/CIT catalog was used for the source parameters. Preliminary regressions that did not include the $\delta c_{0,e}$ term showed significant differences in $\delta c_{1,e}$ between northern and southern CA at small frequencies. It was found that these differences were caused by a noticeable bias in the total residuals of BA18 between northern and southern CA for small magnitude events. Chiou et al. (2010) made a similar observation for the total residuals of CY08: they found a regional difference in median ground-motion amplitude between north and south CA earthquakes which was more noticeable at small magnitude events. The results in section 4 show that the difference in the median ground-motion of small events between northern and southern CA is approximately 0.4 in natural-log units at frequencies between 0.2 and 5.0 Hz . At frequencies well below the corner frequency, a unit change in magnitude leads to a factor of 32 change in the amplitude of the ground motion; thus, a 0.4 natural-log difference in ground motion can be caused by a 0.11 bias in the magnitude estimation between the NCSN and SCSN networks, which could be due to different assumptions in the velocity models or other input parameters used to determine the magnitude of an event. Given the assumption of magnitude bias, the $\delta c_{0,e}$ term is not applied to events less than $M 5$. The source parameters of the moderate-to-large events in NGAWest2 were estimated with fault inversions using data from global networks, and therefore, the potential magnitude bias between the NCSN and SCSN networks is not applicable to events larger than $M 5$. However,

Table 1: Vertices of Northern and Southern CA regions for $\delta_{c_0,e}$

Northern CA		Southern CA	
lat. (deg)	lon. (deg)	lat. (deg)	lon. (deg)
34.5175	-121.5250	37.9775	-116.6225
39.8384	-125.2341	35.2944	-113.4142
41.3595	-124.1684	31.4772	-115.0250
41.3995	-120.7227	31.0082	-117.6898
37.9775	-116.6225	34.5175	-121.5250

this issue should be further investigated in future studies to find the exact cause of this regional difference.

3.1.2 Path Scaling

The functional form for f_P is:

$$f_P = c_4 \ln(R_{rup} + c_5 \cosh(c_6 \max(M - c_{hm}, 0))) + (-0.5 - c_4) \ln(\hat{R}) + \vec{c}_{ca,p}(\vec{x}_c) \cdot \Delta \vec{R} \quad (4)$$

where $\hat{R} = \sqrt{R_{rup}^2 + 50^2}$. The coefficient c_4 , which corresponds to the geometrical attenuation, manages how the ground motion attenuates at short distances. The coefficient c_5 describes the short-distance saturation, this term increases the effective distance for large magnitudes to capture the finite-fault effects (i.e. as the earthquake magnitude increases, the size of the rupture increases resulting in more seismic waves coming from more distant segments of the rupture leading to a larger effective rupture distance). Coefficients c_4 and c_6 control the magnitude saturation at short distances. Full saturation at zero distance is achieved when $c_2 = -c_4 c_6$ is satisfied, non full saturation (i.e. positive magnitude scaling) is achieved when $c_2 > -c_4 c_6$. At distances greater than $50km$, the term $(-0.5 - c_4)$ cancels the empirically estimated geometrical attenuation and fixes it to 0.5 which is the theoretical geometrical attenuation of surface waves. To maintain proper distance scaling and magnitude saturation in the non-ergodic model, all the aforementioned coefficients were fixed to their BA18 values. The non-ergodic distance scaling is captured with the cell-specific anelastic attenuation.

The anelastic attenuation is modeled with the cell-specific anelastic approach, first proposed by Dawood and Rodriguez-Marek (2013) and then extended by Kuehn et al. (2019) and Abrahamson et al. (2019). In this method, the states of California and Nevada are broken into $25 \times 25km$ cells and, for each record, the ray path which connects the site (\vec{x}_s) to the closest point on the rupture (\vec{x}_{cls}) is broken into cell-path segments (ΔR_i) which are lengths of the ray within each cell. For each record, the sum of cell-path segment lengths $\sum_{i=0}^{N_c} \Delta R_i$, is equal to R_{rup} .

The cell-specific anelastic attenuation is modeled by $\Delta \vec{c}_{ca,p} \cdot \Delta \vec{R}$ where $\vec{c}_{ca,p}$ is vector containing the attenuation coefficients of all the cells. In this GMM, $\vec{c}_{ca,p}$ is modeled so that, in areas away from past paths it reverts to c_7 which is the anelastic attenuation coefficient in BA18, making the anelastic attenuation of the non-ergodic model equal to the anelastic attenuation of BA18 ($\vec{c}_{ca,p} \cdot \Delta \vec{R} = c_7 R_{rup}$); while in areas that are covered by the paths in NGAWest2 dataset, $\vec{c}_{ca,p}$ deviates from c_7 to capture the regional attenuation. Figure 3 shows the cells and the path coverage in the selected subset of the NGA-West2 dataset, as well as, the number of paths per cell.

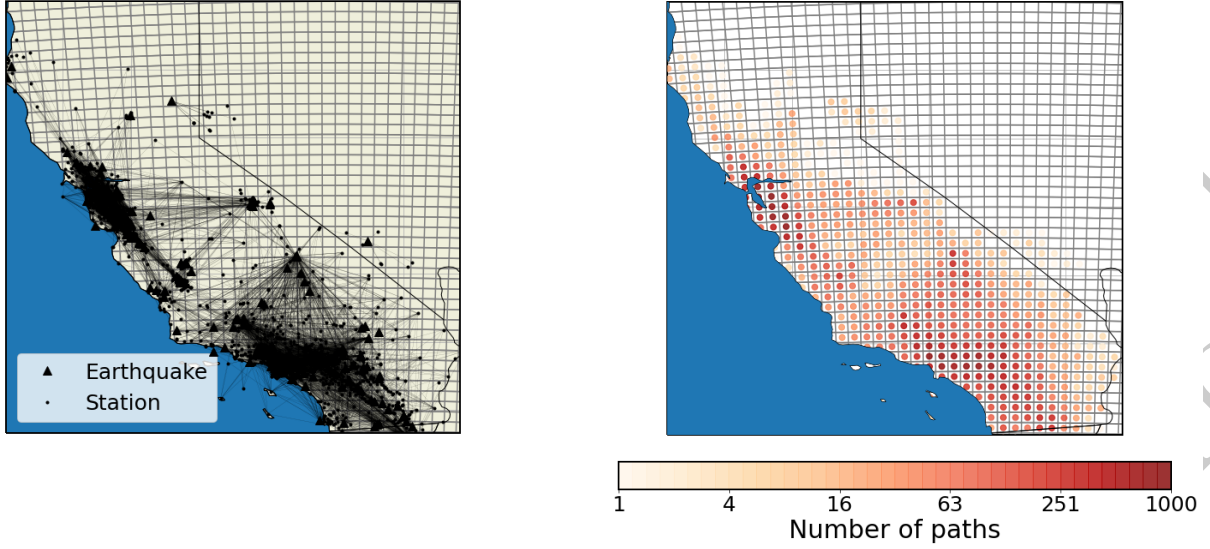


Figure 3: The left figure shows the path coverage for the cell-specific anelastic attenuation in the CA subset of NGAWest2. The right figure shows the number of paths per cell.

3.1.3 Site Scaling

The functional form of the f_S model is:

$$f_S = c_8 \ln \left(\frac{\min(V_{s30}, 1000)}{1000} \right) + f_{NL} + \delta c_{1a,s}(\vec{x}_s) + \delta c_{1b,s} \quad (5)$$

The ergodic components of the site term are: c_8 which controls the V_{S30} scaling of the ground motion, and f_{NL} which is the non-linear site amplification term. The non-ergodic effects related to the site are expressed by the $\delta c_{1a,s}$ and $\delta c_{1b,s}$ coefficients. The station constant, $\delta c_{1a,s}$, which has a finite correlation length, describes the broader adjustments to the backbone model to express the regional site effects. $\delta c_{1b,s}$ has a zero correlation length and acts on top of $\delta c_{1a,s}$ to describe the site specific adjustments. Coefficients with a finite correlation length vary continuously across the domain of interest, whereas coefficients with zero correlation length vary independently from location to location.

The remaining terms f_{ztor} , f_{NM} and f_{Z1} were kept as they are in the ergodic *GMM*.

3.2 Formulation of spatially varying coefficient model

The non-ergodic terms, cell-specific coefficients, and aleatory terms, hereafter collectively called model parameters ($\vec{\theta}$), were estimated by describing the GMM as a hierarchical Bayesian model using the computer software STAN (Stan Development Team, 2019). In Bayesian statistics, the posterior distribution of the parameters is proportional to the likelihood times the prior distribution of the parameters:

$$p(\vec{\theta}|y, x) \propto \mathcal{L}(\vec{\theta})p(\vec{\theta}) \quad (6)$$

The prior distributions are the distributions that the model parameters are assumed to follow in the absence of data; the likelihood function, in general terms, is the probability of observing

Table 2: Summary of model parameters and hyper-parameters

Group Name	Group Notation	Components
Model parameters	$\vec{\theta}$	$\delta c_0, \delta c_{0,e}, \delta c_{1,e}, \delta c_{1a,s}, \delta c_{1b,s},$ $c_{ca,p}, \delta W S_{e,s}^0, \delta B_e^0$
Model hyperparameters	$\vec{\theta}_{hyp}$	$\ell_{1,e}, \omega_{1,e}, \ell_{1a,s}, \omega_{1b,s}, \omega_{1b,s},$ $\ell_{ca1,p}, \omega_{ca1,p}, \omega_{ca2,p}, \phi_0, \tau_0$

the data given the model parameters; and the posterior distributions are the model-parameter distributions informed by the data.

The likelihood can be estimated from the density function of the ground motion:

$$\mathcal{L}(\vec{\theta}) = pdf(\vec{y}|f(x, \vec{\theta}), \phi_0^2 + \tau_0^2) \quad (7)$$

where $f(x, \vec{\theta})$ is the functional form for the median non-ergodic ground-motion:

$$f(x, \vec{\theta}) = (f_{erg}(M, R_{rup}, V_{S30}, \dots) - c_7 R_{rup}) + \delta c_0 + \delta c_{0,e} + \delta c_{1,e} + \delta c_{1a,s} + \delta_{1b,s} + \vec{c}_{ca,p} \cdot \Delta \vec{R} \quad (8)$$

It is equal to the ergodic backbone model without the effect of anelastic attenuation ($f_{erg}(M, R_{rup}, V_{S30}, \dots) - c_7 R_{rup}$), plus the non-ergodic spatially varying constants that have been described the previous section (δc_i), and the cell-specific anelastic attenuation $\vec{c}_{ca,p} \cdot \Delta \vec{R}$.

The model is called hierarchical because the prior distributions are defined in multiple levels. At the lower level, $\vec{\theta}$ follow some prior distributions, which are defined in terms of a different set of parameters, hereafter called hyper-parameters $\vec{\theta}_{hyp}$, which, in turn, either follow some other prior distributions, or they are fixed. In this study, the non-ergodic ergodic regression was performed in two phases: in the first phase, which included a smaller number of frequencies, $\vec{\theta}_{hyp}$ were defined by their own prior distributions that are described later in this section, whereas, in the second phase, most of $\vec{\theta}_{hyp}$ were fixed to their smoothed values, estimated from first phase, and the remaining hyperparameters were left free to follow the same prior distributions as in the first phase. The main reasons for fixing $\vec{\theta}_{hyp}$ in the second phase were to ensure that there are no abrupt changes in the non-ergodic terms between frequencies, to constrain the model to a more physical behavior, and to reduce the computational cost of the second phase which included more frequencies. Table 2 summarizes the parameters that were classified as $\vec{\theta}$ and $\vec{\theta}_{hyp}$; the parameters composing $\vec{\theta}$ have been defined in Section 3.1, the hyper-parameters composing $\vec{\theta}_{hyp}$ have defined later in this section. Table 3 summarizes the $\vec{\theta}_{hyp}$ that were free at each phase. If $\vec{\theta}_{hyp}$ is free, the prior distribution of a model parameter, θ_i , can be explicitly defined in terms of $\vec{\theta}_{hyp}$ as follows:

$$p(\theta_i) = f(\theta_i)d\theta_i = \left(\int f(\theta_i|\vec{\theta}_{hyp})f(\vec{\theta}_{hyp}) d\vec{\theta}_{hyp} \right) d\theta_i \quad (9)$$

More specifically, the δc_0 constant has a normal prior distribution with a zero mean and a 0.1 standard deviation:

$$\delta c_0 \sim \mathcal{N}(0, 0.1) \quad (10)$$

Table 3: Free hyper-parameters at each regression phase

Phase	Free hyper-parameters
1	$\ell_{1,e}, \omega_{1,e}, \ell_{1a,s}, \omega_{1a,s}, \omega_{1b,s}, \ell_{ca1,p}, \omega_{ca1,p}, \omega_{ca2,p}, \phi_0, \tau_0$
2	ϕ_0, τ_0

The mean is set to zero because in absence of data, there should be no shift between the ergodic and non-ergodic GMM. The standard deviation is small because any constant shift informed by the regional data or the re-weighting of the residuals is expected to be small.

For earthquakes with magnitudes less than M 5 and frequencies less than 5 Hz , $\delta c_{0,e}$ follow a normal prior distribution with a zero mean and a 0.2 standard deviation. Preliminary analyses, which did not include $\delta c_{0,e}$, had a 0.2 to 0.4 regional difference in $\delta c_{1,e}$ between northern and southern California, which have a 16 and 3% probability of being exceeded the selected standard deviation. Therefore, the posterior distribution of $\delta c_{0,e}$ will deviate from zero to reach a similar range only if there is significant support by the data; otherwise, $\delta c_{0,e}$ will stay close to zero implying no systematic difference between northern and southern CA at small magnitude events.

$$\delta c_{0,e} \sim \begin{cases} 0 & \text{for } M > 5 \text{ or } f > 5Hz \\ \mathcal{N}(0, 0.2) & \text{for } M < 5 \text{ and } f < 5Hz \end{cases} \quad (11)$$

The non-ergodic constants $\delta c_{1,e}(\vec{x}_e)$ and $\delta c_{1a,s}(\vec{x}_s)$ follow multivariate normal prior distributions with zero mean and Matern (negative exponential) covariance functions (κ). κ imposes the spatial correlation on $\delta c_{1,e}$ and $\delta c_{1a,s}$: it ensures that the values of $\delta c_{1,e}$ and $\delta c_{1a,s}$ will be similar for earthquakes or sites in close proximity and that $\delta c_{1,e}$ and $\delta c_{1a,s}$ would vary continuously from location to location.

$$\begin{aligned} \delta c_{1,e} &\sim \mathcal{N}(0, \kappa_{1,e}) \\ \delta c_{1a,s} &\sim \mathcal{N}(0, \kappa_{1a,s}) \end{aligned} \quad (12)$$

The covariance function between a pair of earthquakes for $\kappa(\vec{x}_e, \vec{x}'_e)$ or between a pair of stations for $\kappa(\vec{x}_s, \vec{x}'_s)$ is defined in equation (13); \vec{x} and \vec{x}' are the coordinates of the two earthquakes or sites depending on the coefficient, ω_i is the standard deviation, and ℓ_i is the correlation length. ω_i controls the variability of the non-ergodic coefficients, that is, how much the values of the coefficients could vary between locations that are far from each other. ℓ_i governs the length scale of the spatial variation of δc_i ; increasing ℓ_i makes δc_i to vary more gradually with distance.

$$\begin{aligned} \kappa_{1,e}(\vec{x}_e, \vec{x}'_e) &= \omega_{1,e}^2 e^{-\frac{\|\vec{x}_e - \vec{x}'_e\|}{\ell_{1,e}}} \\ \kappa_{1a,s}(\vec{x}_s, \vec{x}'_s) &= \omega_{1a,s}^2 e^{-\frac{\|\vec{x}_s - \vec{x}'_s\|}{\ell_{1a,s}}} \end{aligned} \quad (13)$$

Both $\ell_{1,e}$ and $\ell_{1a,s}$ have inverse gamma prior distributions with distribution parameters α and β equal to 2 and 50 which corresponds to a mode and mean of 16.7 and 50 km , respectively.

$$\begin{aligned} \ell_{1,e} &\sim InvGamma(2.0, 50.0) \\ \ell_{1a,s} &\sim InvGamma(2.0, 50.0) \end{aligned} \quad (14)$$

Inverse gamma distributions are defined only for positive real numbers which is a desirable property for the prior distributions of the correlation lengths as negative correlation lengths do not have any

physical meaning. The $\ell_{1,e}$ and $\ell_{1a,s}$ correlation lengths are expected to be around 10 to 50 *km*, where the inverse gamma distribution has most of its mass, but larger values are also possible, if they are supported by the data, due to its exponential tail.

The prior distribution of $\omega_{1,e}$ and $\omega_{1a,s}$ is an exponential distribution with a rate of 20

$$\begin{aligned}\omega_{1,e} &\sim \text{exp}(20) \\ \omega_{1a,s} &\sim \text{exp}(20)\end{aligned}\tag{15}$$

These prior distributions were chosen for $\omega_{1,e}$ and $\omega_{1a,s}$ to penalize unnecessary model complexity (Simpson et al., 2017). A ω_i equal to zero implies no variability for δc_i , meaning that there are no systematic effects related to that parameter. In an exponential distribution, most of the mass is near zero, which allows δc_i to deviate from zero to capture systematic effects related to that parameter only if there is significant support by the ground-motion observations. For the same reason, exponential prior distributions were used in Kuehn et al. (2020) to model the standard deviations of the regional terms in the KBCG20 partially non-ergodic subduction-zone GMM.

The site-specific adjustment, $\delta c_{1b,s}$, follows a normal distribution with a zero mean and a $\omega_{1b,s}$ standard deviation:

$$\delta c_{1b,s} \sim \mathcal{N}(0, \omega_{1b,s})\tag{16}$$

$\delta c_{1b,s}$ is a function of the site location, the same adjustment is applied to all ground motions recorded at the same station.

The prior distribution for $\omega_{1b,s}$ is a log-normal distribution with a logmean of -0.8 and a standard deviation of 0.3 natural log units:

$$\omega_{1b,s} \sim \mathcal{LN}(-0.8, 0.3)\tag{17}$$

This prior distribution has a median value of 0.45 , and a 16^{th} and 84^{th} percentile of 0.33 and 0.6 , respectively. Bayless and Abrahamson (2019b) found ϕ_{S2S} to range from 0.4 to 0.6 which is consistent with the prior distribution for $\omega_{1a,s}$.

The prior distribution of $\vec{c}_{ca,p}$ is a multivariate normal distribution with an upper truncation limit at zero:

$$\vec{c}_{ca,p} \sim \mathcal{N}(\mu_{ca,p}, \kappa_{ca,p})\mathcal{T}(, 0)\tag{18}$$

where $\mu_{ca,p}$ is the mean of the distribution, and $\kappa_{ca,p}$ is the covariance function. To ensure the physical extrapolation of the GMM, $\vec{c}_{ca,p}$ is limited to be less or equal to zero, which is satisfied by setting the upper limit of the normal distribution at zero ($\mathcal{T}(, 0)$). Two key differences from the Abrahamson et al. (2019) approach when modeling the cells are the different mean and the different covariance function of the prior distribution. In this model, the mean of the prior is equal to the value of the anelastic-attenuation coefficient in Bayless and Abrahamson (2019b) ($\mu_{ca,p} = c_{7\ BA18}$); thus, in areas with sparse data, the non-ergodic attenuation goes back to the ergodic attenuation to ensure reasonable extrapolation at large distances. This decision was made because the local data may not be sufficient to estimate both the median shift and the spatial variability of the anelastic attenuation. The covariance function (equation (19)) is the sum of a Matern kernel scaled by $\omega_{ca1,p}^2$ and a diagonal kernel scaled by $\omega_{ca2,p}^2$. The Matern kernel controls the underlining continuous variation of anelastic attenuation over large areas, whereas, the diagonal kernel allows for some independence in the attenuation from cell to cell. $\omega_{ca1,p}$ controls the size of the underling variability of $c_{ca,p}$ over large distances, the correlation length $\ell_{ca1,p}$ controls how fast the underling component

of $c_{ca,p}$ varies with distance, and $\omega_{ca2,p}$ controls the size of the independent variability. The location of each cell is defined in terms of its midpoint coordinates, \vec{c}_c ; the distance between the cells is calculated by the L2 norm of the vector between midpoints of the cells.

$$\kappa_{ca,p}(\vec{x}_c, \vec{x}'_c) = \omega_{ca1,p}^2 e^{-\frac{\|\vec{x}_c - \vec{x}'_c\|}{\ell_{ca1,p}}} + \omega_{ca2,p}^2 \delta(\|\vec{x}_c - \vec{x}'_c\|) \quad (19)$$

$\ell_{ca1,p}$ has an inverse gamma distribution with the same parameters as the prior distributions for ℓ_{1e} and $\ell_{1a,s}$. $\omega_{ca1,p}$ and $\omega_{ca2,p}$ have an exponential prior distribution with the same parameters as the prior distributions for $\omega_{1,e}$ and $\omega_{1a,s}$.

$$\begin{aligned} \ell_{ca,p} &\sim \text{InvGamma}(2.0, 50.0) \\ \omega_{ca1,p} &\sim \text{exp}(20) \\ \omega_{ca2,p} &\sim \text{exp}(20) \end{aligned} \quad (20)$$

The non-ergodic within-event residuals, $\delta W_{e,s}^0$, follow a normal distribution with a zero mean and ϕ_0 standard deviation.

$$\delta W_{e,s}^0 \sim \mathcal{N}(0, \phi_0^2) \quad (21)$$

The prior distribution of ϕ_0 is a log-normal distribution with a logmean of -1.3 and a standard deviation of 0.3 natural log units (equation (22)). This set of parameters leads to a prior mean of 0.27 and a 16^{th} to 84^{th} percentile range of 0.2 to 0.37 . BA18 is an ergodic model, and so an estimate of ϕ_0 is not available to inform the prior distribution of ϕ_0 of this model. However, ϕ_{SS} , which is available in BA18, is about 0.4 for most frequencies, and because ϕ_0 is smaller than ϕ_{SS} by definition (Al Atik et al., 2010), the range of the prior distribution is reasonable.

$$\phi_0 \sim \mathcal{LN}(-1.3, 0.3) \quad (22)$$

The non-ergodic between-event residuals, δB_e^0 , follow a normal distribution:

$$\delta B_e^0 \sim \mathcal{N}(0, \tau_0) \quad (23)$$

with a zero mean and τ_0 standard deviation. δB_e^0 is a function of the earthquake id, e ; that is, the same δB_e^0 is applied to all recordings of the same earthquake.

The prior distribution of τ_0 is a log-normal distribution with a -1.0 logmean and 0.3 log-standard deviation.

$$\tau_0 \sim \mathcal{LN}(-1.0, 0.3) \quad (24)$$

The τ_0 distribution parameters are judged to be reasonable because the mean and 16^{th} and 84^{th} percentiles (0.38 , 0.27 and 0.50) are in agreement with other non-ergodic studies where the total non-ergodic standard deviation ($\sqrt{\phi_0^2 + \tau_0^2}$) ranges from 0.36 to 0.55 .

3.3 Predictive distributions of coefficients at new locations

The non-ergodic coefficients can be estimated at new locations (\vec{x}^*) by conditioning them on the non-ergodic coefficients at the existing locations (\vec{x}); that is, the location of stations or past events depending on the coefficient. Since all non-ergodic coefficients follow multivariate normal distributions, for known values of the non-ergodic coefficients ($\delta \vec{c}_i$) at the \vec{x} , the non-ergodic

coefficients at \vec{x}^* also follow multivariate normal distributions with the mean and covariance matrix (Rasmussen and Williams, 2006; Landwehr et al., 2016):

$$\vec{\mu}_{\delta c_i^*|\delta c_i} = \mathbf{k}_i^\top \mathbf{K}_i^{-1} \vec{\delta c}_i \quad (25)$$

$$\Psi_{\delta c_i^*|\delta c_i} = \mathbf{K}^*_{i} - \mathbf{k}_i^\top \mathbf{K}_i^{-1} \mathbf{k}_i \quad (26)$$

where $\vec{\mu}_{\delta c_i^*|\delta c_i}$ mean of non-ergodic ergodic coefficients at \vec{x}' conditioned on $\vec{\delta c}_i$, $\Psi_{\delta c_i^*|\delta c_i}$ is the covariance of non-ergodic coefficients at \vec{x}' conditioned on $\vec{\delta c}_i$, \mathbf{K} is the covariance between the non-ergodic coefficients at the existing locations ($\mathbf{K}_i = \kappa_i(\vec{x}, \vec{x})$), \mathbf{k} is the covariance between the non-ergodic coefficients at the existing and new locations ($\mathbf{k}_i = \kappa_i(\vec{x}, \vec{x}^*)$), and \mathbf{K}^* is the covariance between the non ergodic coefficients at the new locations ($\mathbf{K}^*_i = \kappa_i(\vec{x}^*, \vec{x}^*)$).

However, the non-ergodic coefficients at \vec{x} are not perfectly known. There is some epistemic uncertainty associated with $\vec{\delta c}_i$ which is quantified by their posterior distribution. To simplify the calculations and obtain a closed-form solution, $\vec{\delta c}_i$ is assumed to follow a multivariate normal posterior distribution ($\vec{\delta c}_i \sim \mathcal{N}(\vec{\mu}_{\delta c_i}, \Psi_{\delta c_i})$); $\vec{\mu}_{\delta c_i}$ is the posterior mean, and $\Psi_{\delta c_i}$ is a diagonal matrix with the posterior variances across the diagonal. We consider this assumption to be reasonable because all $\vec{\delta c}_i$ have multivariate normal prior distributions. If all of the hyper-parameters were fixed, the posterior distributions of $\vec{\delta c}_i$ would indeed be multivariate normal distributions, but because some of the hyper-parameters are free, the posterior distributions of $\vec{\delta c}_i$ may slightly deviate from the assumption. The epistemic uncertainty of δc_i can be included in the δc_i^* predictions by using the marginal distribution of δc_i^* :

$$p(\delta c_i^*) = \int p(\delta c_i^*|\delta c_i) p(\delta c_i) d\delta c_i \quad (27)$$

Due to the previous assumption, $p(\delta c_i^*)$ is also a multivariate normal distribution with mean and covariance matrix given in Equations (28) and (29), respectively (Bishop, 2006).

$$\vec{\mu}_{\delta c_i^*} = \mathbf{k}_i^\top \mathbf{K}_i^{-1} \vec{\mu}_{\delta c_i} \quad (28)$$

$$\Psi_{\delta c_i^*} = \mathbf{K}^*_{i} - \mathbf{k}_i^\top \mathbf{K}_i^{-1} \mathbf{k}_i + \mathbf{k}_i^\top \mathbf{K}_i^{-1} \Psi_{\delta c_i} (\mathbf{k}_i^\top \mathbf{K}_i^{-1})^\top \quad (29)$$

3.4 Inter-frequency Correlation

The main motivation behind the development of this non-ergodic EAS GMM is to use it with RVT to create an equivalent non-ergodic *PSA* GMM; in doing this, it is important to capture the inter-frequency correlation of the non-ergodic terms, otherwise, as it was demonstrated by Bayless and Abrahamson (2018), the variability of the *PSA* values is underestimated. The correlation coefficient (ρ) is a measure of the linear relationship of two random variables X_1 and X_2 . A ρ that is equal to one implies that X_2 can be perfectly defined as a linear function of X_1 , and vice versa; a zero ρ implies that the two random variables are uncorrelated. In ground-motion studies, the inter-frequency correlation coefficient is a measure of the width of the peaks and troughs of a *PSA* or *EAS* spectrum: the stronger the correlation of the amplitudes between frequencies, the wider the peaks and troughs of the spectra will be.

The correlation coefficient for a non-ergodic term δc_i , at frequencies f_1 and f_2 , is defined as:

$$\rho_{\delta c_i}(f_1, f_2) = \frac{cov(\delta c_i(f_1), \delta c_i(f_2))}{\sigma_{\delta c_i(f_1)} \sigma_{\delta c_i(f_2)}} \quad (30)$$

where cov is the covariance of δc_i at the two frequencies, and σ_i is the standard deviation of δc_i . ρ can be determined from the data using the maximum likelihood estimator (Kutner et al., 2005):

$$\rho_{\delta c_i}(f_1, f_2) = \frac{\sum_{j=1}^n (\delta c_{i,j}(f_1) - \bar{\delta c}_i(f_1)) (\delta c_{i,j}(f_2) - \bar{\delta c}_i(f_2))}{\sqrt{\sum_{j=1}^n (\delta c_{i,j}(f_1) - \bar{\delta c}_i(f_1))^2} \sqrt{\sum_{j=1}^n (\delta c_{i,j}(f_2) - \bar{\delta c}_i(f_2))^2}} \quad (31)$$

where n is the number of observations, $\delta c_{i,j}$ is the j^{th} sample of δc_i , and $\bar{\delta c}_i$ is the mean value of δc_i . For a large number of samples ($n > 25$), ρ can be transformed into a random variable z that follows a normal distribution with equation (32) (Kutner et al., 2005); the standard deviation of z is given in equation (33).

$$z = \tanh^{-1}(\rho) = \frac{1}{2} \ln \left(\frac{1 + \rho}{1 - \rho} \right) \quad (32)$$

$$\sigma(z) = \sqrt{\frac{1}{n - 3}} \quad (33)$$

The same functional form that was used to model the correlation of the total EAS residuals in Bayless and Abrahamson (2019a) was used here to fit the empirical correlations of the non ergodic terms:

$$\rho(f_r) = \begin{cases} 1 & \text{for } f_r = 0 \\ \tanh(Ae^{Bf_r} + Ce^{Df_r}) & \text{for } f_r \neq 0 \end{cases} \quad (34)$$

$$f_r = \left| \ln \left(\frac{f_1}{f_2} \right) \right| \quad (35)$$

A , B , C , D are the model parameters, and f_r is the absolute value of the natural log of the ratio of the two frequencies. This functional form allows for a two-term exponential decay as a function of the logarithm of frequency; this behavior is required because both the correlation of the total residuals in Bayless and Abrahamson (2019a) and the correlation of the epistemic uncertainty terms presented in section 4 exhibit a steep decay at frequencies near the conditioning frequency which then flattens at frequencies that are further from the conditioning frequency. The model parameters were estimated with a non-linear least-squares regression on z using the MINPACK.LM package (Elzhov et al., 2016) in the statistical software R (R Core Team, 2020); $\sigma(z)$ was used as weights in the least-squares regression emphasising the fit to the higher correlation values which have more samples.

In this study, one difference from the Bayless and Abrahamson (2019a) is it that the inter-frequency correlation of all epistemic uncertainty terms was modeled as frequency independent (i.e. A , B , C , D are constants). This was done, because at it can be seen in section 4, $\delta c_{1a,s}$ and $\delta c_{1b,s}$, which are the biggest contributors to the total non-ergodic effects, have an almost frequency independent inter-frequency correlation. $\vec{c}_{ca,p}$ show the most noticeable frequency dependence in inter-frequency correlation, but it becomes more stable at intermediate and large frequencies which is the frequency range where it has the biggest impact. The assumption of frequency independence should be re-examined in future studies with a larger dataset.

4 Results

4.1 Hyperparameters

Figure 4 presents the mean, 5th and 95th percentiles of the posterior distribution of the hyperparameters of the non-ergodic terms; the proposed smoothed values are also presented in the same figure. As mentioned in section 3.2, the regression for this model was performed in two phases; in the first phase, all model hyperparameter were free and estimated based on the data and prior distributions, whereas in the second phase, the hyper-parameters of the non-ergodic terms were fixed to their smoothed values, and τ_0 and ϕ_0 were reestimated for the new set of smoothed hyper-parameters.

Figure 4a shows the variation of the correlation length for $\delta c_{1,e}$ with frequency. The posterior distribution of $\ell_{1,e}$ is wide due to the small number of earthquakes. Overall, the mean estimate of $\ell_{1,e}$ is around 40km except at low frequencies where at 0.3Hz it jumps up to 85km. Because there is no reason for $\ell_{1,e}$ to increase at low frequencies, it was fixed to the average $\ell_{1,e}$ over all frequencies, as it the simplest model. Furthermore, there are less data at low and high frequencies making the estimates of the hyperparameters at these frequency ranges less stable.

Figure 4b shows how $\omega_{1,e}$ changes with frequency. In this case, the posterior mean of $\omega_{1,e}$ stays constant at low and intermediate frequencies, and it exhibits an increase at high frequencies. Similarly to $\ell_{1,e}$, there is no reason for $\omega_{1,e}$ to increase at high frequencies so it was fixed to the average value over all frequencies. One possible cause of the apparent increase of $\omega_{1,e}$ at high frequencies is that some of the non-ergodic site effects could have been mapped into non-ergodic source effects in the regression. It is expected that the non-ergodic site effects will increase at high frequencies because the regional differences in site amplification tend to have a larger impact on the high frequencies. This assumption is consistent with the behavior of $\omega_{1a,s}$ and $\omega_{1b,s}$, which both show an increase with frequency. For this reason, the difference between the estimated and smoothed $\omega_{1,e}$ was moved to $\omega_{1a,s}$.

In smoothing $\omega_{1a,s}$, up to the frequency of 15Hz, a piece-wise linear model was fit to the estimated mean values; whereas beyond 15Hz, it was fit to the square root of the sum of squares of the estimated mean $\omega_{1a,s}$ and the difference between the estimated mean and smoothed $\omega_{1,e}$. Minimal smoothing was applied to $\ell_{1a,s}$ and $\omega_{1b,s}$ as they show a relatively small variation between neighbouring frequencies.

The smoothed $\ell_{ca1,p}$ was fixed to the average of the mean estimates that are less than 75km; this upper limit was imposed because the $\ell_{ca1,p}$ with large mean estimates also had wide posterior distributions, meaning that $\ell_{ca1,p}$ could not be reliably estimated at those frequencies.

$\omega_{ca1,p}$ and $\omega_{ca2,p}$ exhibit similar characteristics in their variation with frequency: they are very small at low frequencies, they show an approximately linear increase with the log of frequency at intermediate frequencies, and they reach a plateau at high frequencies. This happens because the effects of anelastic attenuation are more noticeable at high frequencies, and likewise, spatial changes in the anelastic attenuation will have a larger effect on higher frequencies. This behavior was also observed by Kuehn et al. (2019) who found that the standard deviation of the cell-specific attenuation coefficients of their non-ergodic PSA GMM was smaller at long periods .

Figure 5 presents the terms that were reestimated in the second step. The coefficient δc_0 corresponds to the shift of the non-ergodic GMM due to the reweighting of the residuals. For most frequencies, the change in the constant from the ergodic model is less than 10%. The regional constant $\delta c_{0,e}$, which corrects for the bias due to the differences in the small magnitude conversion, is about 0.4 for the northern California and zero for the southern California. In the NGAWest2

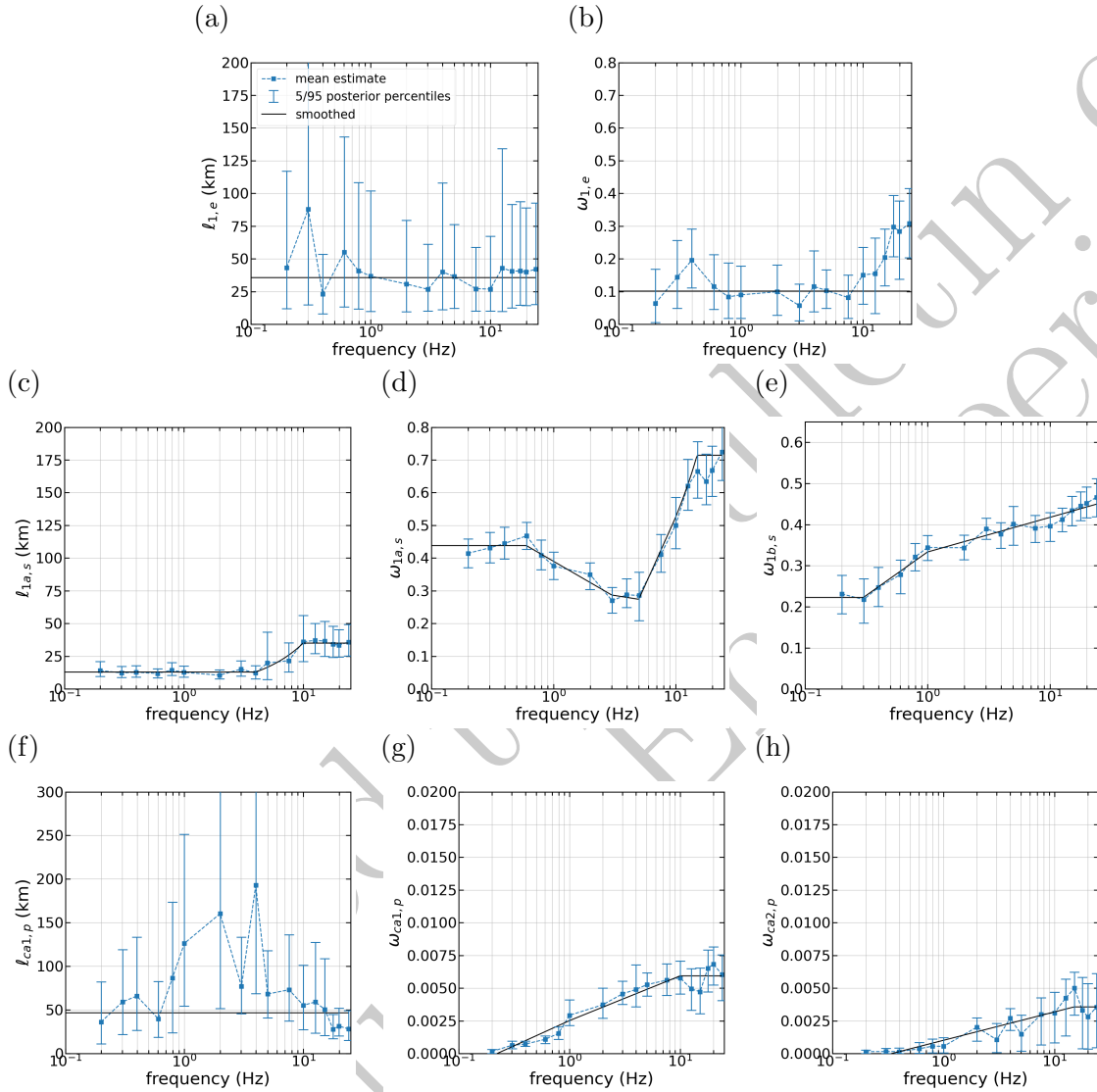


Figure 4: Estimated and smoothed hyperparameters versus frequency; the circular line depicts the mean estimate of the hyperparameters from the original regression, the vertical bars correspond to the 5/95 percentiles of the posterior distribution, and the solid line represent to the smoothed hyperparameters. (a) correlation length of the source constant, $\ell_{1,e}$, (b) standard deviation of source constant, $\omega_{1,e}$, (d) correlation length of the site constant with finite correlation length, $\ell_{1a,s}$, (e) standard deviation of the site constant with finite correlation length, $\omega_{1a,s}$, (c) standard deviation of the site term with zero correlation length, $\omega_{1b,s}$, (f) correlation length of the cell-specific anelastic attenuation, $\ell_{ca1,p}$, (g) standard deviation of the uncorrelated component of the cell-specific anelastic attenuation, $\omega_{ca1,p}$, and (h) standard deviation of the correlated component of the cell-specific anelastic attenuation, $\omega_{ca2,p}$.

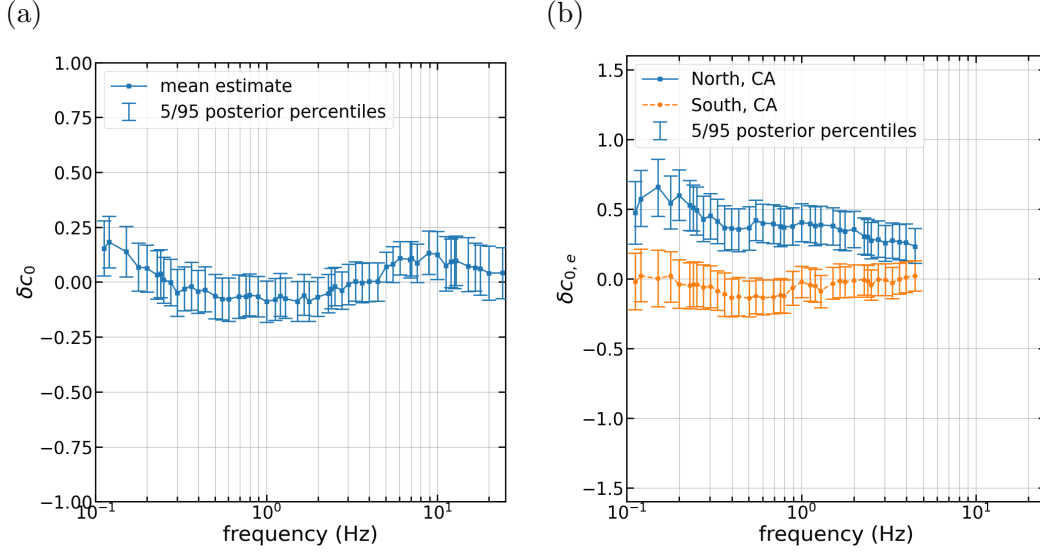


Figure 5: Estimated δc_0 and $\delta c_{0\ N/S}$ versus frequency; the circular marker corresponds to the mean estimate, the vertical bars represents the 5/95 percentiles of the posterior distribution (a) constant shift, δc_0 , (b) regional shift, $\delta c_{0,e}$, the solid line with the square markers corresponds to the Northern CA, the dashed line with the circular markers corresponds to the Southern CA

dataset, most of the data are located in southern California, so it is expected that the base model would be consistent with the southern part of the state with the main correction applied to the northern part of California.

4.2 Spatially varying coefficients and cell-specific anelastic attenuation

Figure 6 shows the spatial distribution of the mean estimate and epistemic uncertainty of $\delta c_{1,e}$, $\delta c_{1a,s}$, and $\delta c_{1b,s}$ for $f = 5\text{Hz}$. As mentioned in Section 3, the $\delta c_{1,e}$ varies as a function of the source coordinates, whereas $\delta c_{1a,s}$ and $\delta c_{1b,s}$ as a function the site coordinates. In areas with past earthquakes, the mean estimate of $\delta c_{1,e}$ deviates from zero and its epistemic uncertainty is small. $\delta c_{1,e}$ is positive if the earthquakes in a region have systematically above average source effects and negative if the source effects are below the average. In areas with sparse or no data, the systematic effects related to the source cannot be reliably estimated, thus, $\delta c_{1,e}$ approaches zero and its epistemic uncertainty is large. The same behavior is observed in the spatial distribution of $\delta c_{1a,s}$: in large metropolitan areas, where most of the station are located, the $\delta c_{1a,s}$ mean estimate deviates from zero, and its epistemic uncertainty is small; in remote areas, the $\delta c_{1a,s}$ mean estimate approaches zero and, its epistemic uncertainty is large. $\delta c_{1b,s}$ is only plotted at the station locations as it has a zero correlation length, meaning that as we move away from a station it will directly go to zero. The mean estimates of $\delta c_{1b,s}$ do not exhibit any spatial correlation (i.e. there are no regions where $\delta c_{1b,s}$ are systematically positive or negative) meaning that spatially correlated component of the site effects was properly captured by $\delta c_{1a,s}$.

Figure 7 illustrates the spatial distribution of the cell-specific anelastic attenuation. The mean of $c_{ca,p}$ deviates from $c_{7\ BA18}$ in cells that are crossed by many paths, whereas it stays close to $c_{7\ BA18}$ in cells crossed by few or zero paths. In addition, cells that are crossed by few paths have large epistemic uncertainty in $c_{ca,p}$. Overall, the epistemic uncertainty is low in Bay Area and Los Angeles and high in the northern part of California and the state of Nevada. The main features

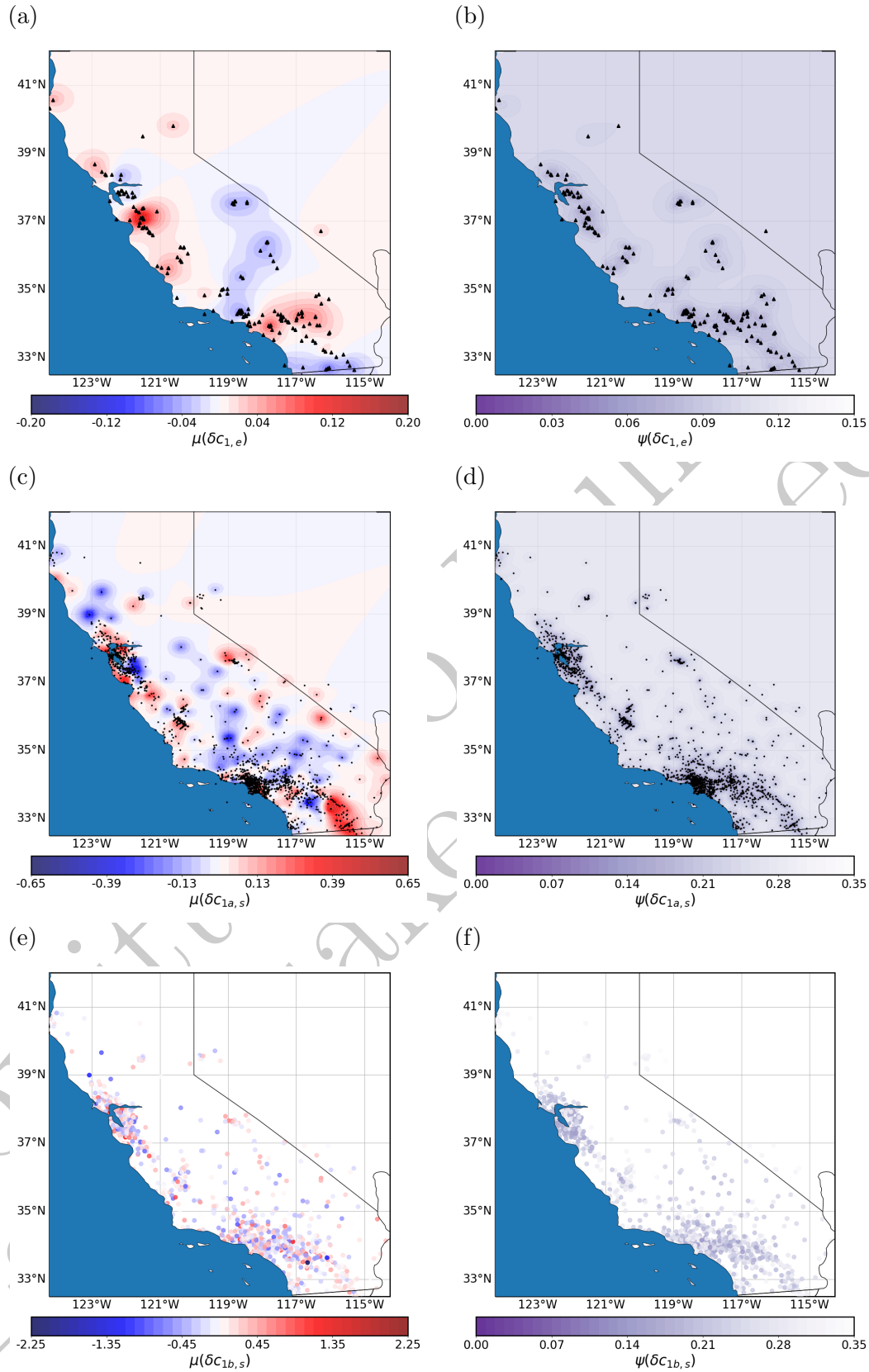


Figure 6: Spatial distribution of source and site constants at $f = 5Hz$. Triangle markers show the location of earthquakes, dots show the location of stations. (a) mean estimate of $\delta c_{1,e}$, (b) epistemic uncertainty of $\delta c_{1,e}$, (c) mean estimate of $\delta c_{1a,s}$, (d) epistemic uncertainty of $\delta c_{1a,s}$, (e) mean estimate of $\delta c_{1b,s}$, and (f) epistemic uncertainty of $\delta c_{1b,s}$.

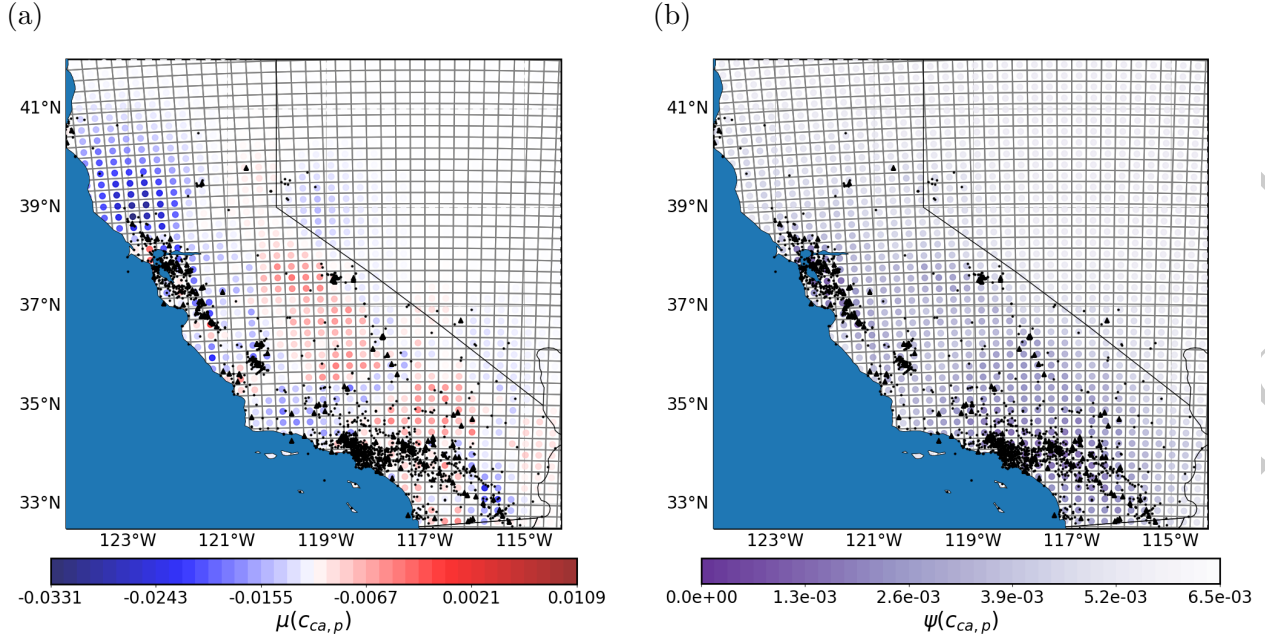


Figure 7: Spatial distribution of cell specific anelastic attenuation at $f = 5 Hz$. (a) mean estimate of $c_{ca,p}$, and (b) epistemic uncertainty of $c_{ca,p}$.

that stand out in Figure 7a are the higher than average anelastic attenuation north of the San Francisco Bay Area and east of San Diego, and the less than average anelastic attenuation in the Central Valley and east of Los Angeles.

These findings are consistent with published attenuation models shown in Figure 8; Figure 8a corresponds to the Eberhart-Phillips (2016) Q model for frequencies 6 to 12 Hz , and 8a corresponds to the Phillips et al. (2014) Q model for the S-waves at 4km depth. The quality factor, Q , is inversely proportional to the anelastic attenuation: high Q means low anelastic attenuation, and vice versa. Both models show small Q values north of Bay Area, and large Q values in Central Valley; additionally, Eberhart-Phillips (2016), which covers the entire state of California and Nevada, shows small values of Q east of San Diego and large values of Q east of Los Angeles. The mean value of $c_{ca,p}$ and the Q model of Eberhart-Phillips (2016) differ in Nevada because there are no paths that cover that region. The large epistemic uncertainty of $c_{ca,p}$ in Nevada means that the cell-specific anelastic attenuation cannot be estimated in that region with the current data set. This comparison shows that the cell specific anelastic attenuation captures an underlying physical behavior.

Figure 9 shows the epistemic uncertainty of the non-ergodic terms as a function of the number of records for $\delta c_{1,e}$, $\delta c_{1a,s}$ and $\delta c_{1b,s}$, and as a function of the number of paths for $c_{ca,p}$. The epistemic uncertainty of $\delta c_{1,e}$ and $\delta c_{1a,s}$ is not sensitive to the number of records, whereas the epistemic uncertainty of $\delta c_{1b,s}$ and $c_{ca,p}$ decreases as the number of records and number of paths increases. This occurs because $\delta c_{1b,s}$ is spatially uncorrelated, and $c_{ca,p}$ has a spatially uncorrelated component; $\delta c_{1b,s}$ can be estimated more accurately as the number of ground motions recorded at a station increases, and $c_{ca,p}$ can be estimated more accurately as the number of paths crossing a cell increases. $\delta c_{1,e}$ and $\delta c_{1a,s}$ are spatially correlated and so the location of an event or a station is also important. That is, $\delta c_{1a,s}$ can have less epistemic uncertainty near a group of stations with few records at each station than near a remote station with a large number of records, if collectively,

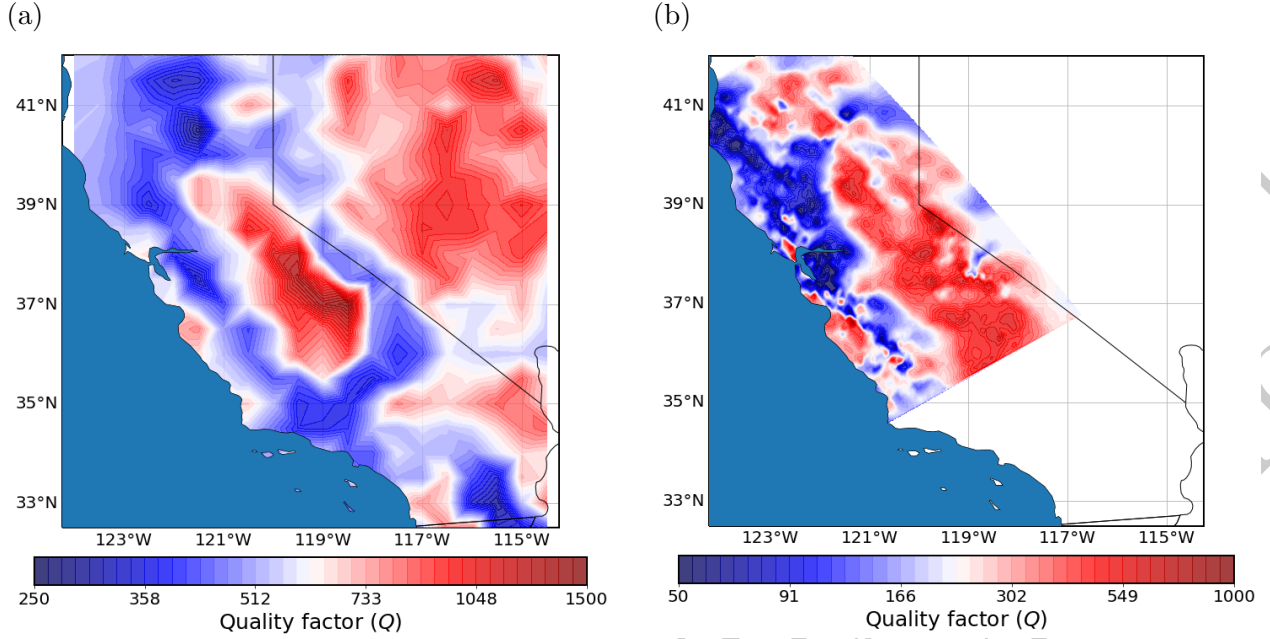


Figure 8: Seismic attenuation models for California from seismic inversions. (a) Phillips et al. (2014) attenuation model for frequencies between 6 and 12 Hz , and (b) Eberhart-Phillips (2016) S-wave attenuation model for northern California at depth of 4 km .

the group of stations has more data to constrain $\delta c_{1a,s}$. The same holds true for $\delta c_{1,e}$ regarding the spatial distribution of events.

4.3 Non-ergodic residuals

The residuals of the non-ergodic model at $f = 5Hz$ are presented in Figure 10: the dots represent the residuals, the solid line corresponds to the moving average, and the error bars correspond to the standard deviation. δB_e^0 shows no trend and an approximately constant standard deviation with magnitude; δW_{es}^0 also shows no trend, but the standard deviation reduces with magnitude. Additionally, δW_{es}^0 shows no trend and a constant standard deviation with R_{rup} and V_{S30}

4.4 Standard deviation

In the model development, for simplicity, the aleatory standard deviations, τ_0 and ϕ_0 , were modeled as magnitude independent. Any magnitude dependence of τ_0 and ϕ_0 was determined in post processing based on the non-ergodic residuals. τ_0 was modeled as constant, as, for the most part, the δB_e^0 residuals did not exhibit any reduction in standard deviation with magnitude (Figure 10). Because the number of events greater than M 6.5 is small, the model for τ_0 did not follow the reduction of the empirical standard deviation at large magnitudes, but instead it followed the standard deviation of the small events. ϕ_0 was modeled as a piece-wise linear function (equation (36)), as δW_{es}^0 residuals exhibit some reduction in the standard deviation with increasing magnitude: ϕ_{0M_1} is the within-event standard deviation for magnitudes less than 5, and ϕ_{0M_2} is the within-event standard deviation for magnitudes greater than 6.5.

The aleatory parameters (τ_0 , ϕ_{0M_1} , and ϕ_{0M_2}) were smoothed in order to ensure that the

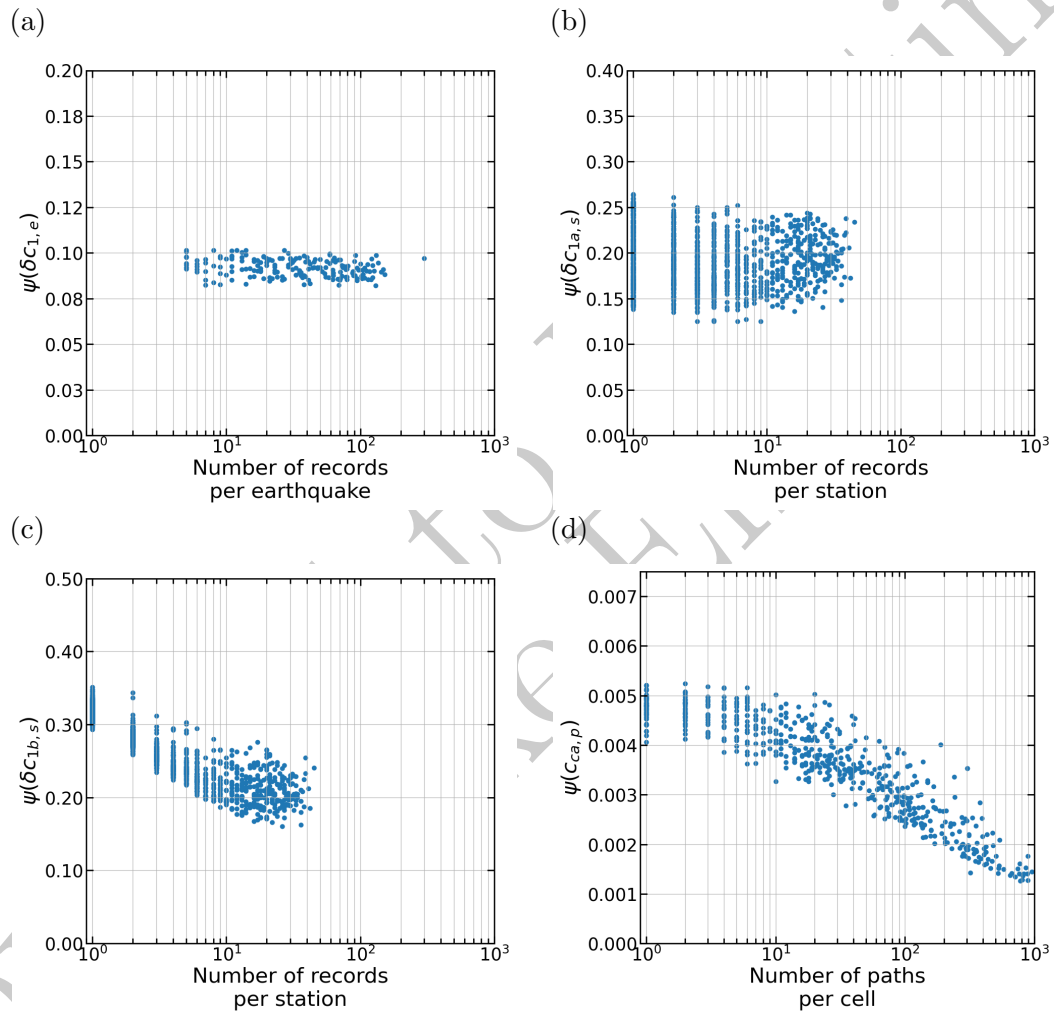


Figure 9: Standard deviations of posterior distributions of non-ergodic terms; (a) $\delta c_{1,e}$, (b) $\delta c_{1a,s}$, (c) $\delta c_{1b,s}$, and (d) $c_{ca,p}$.

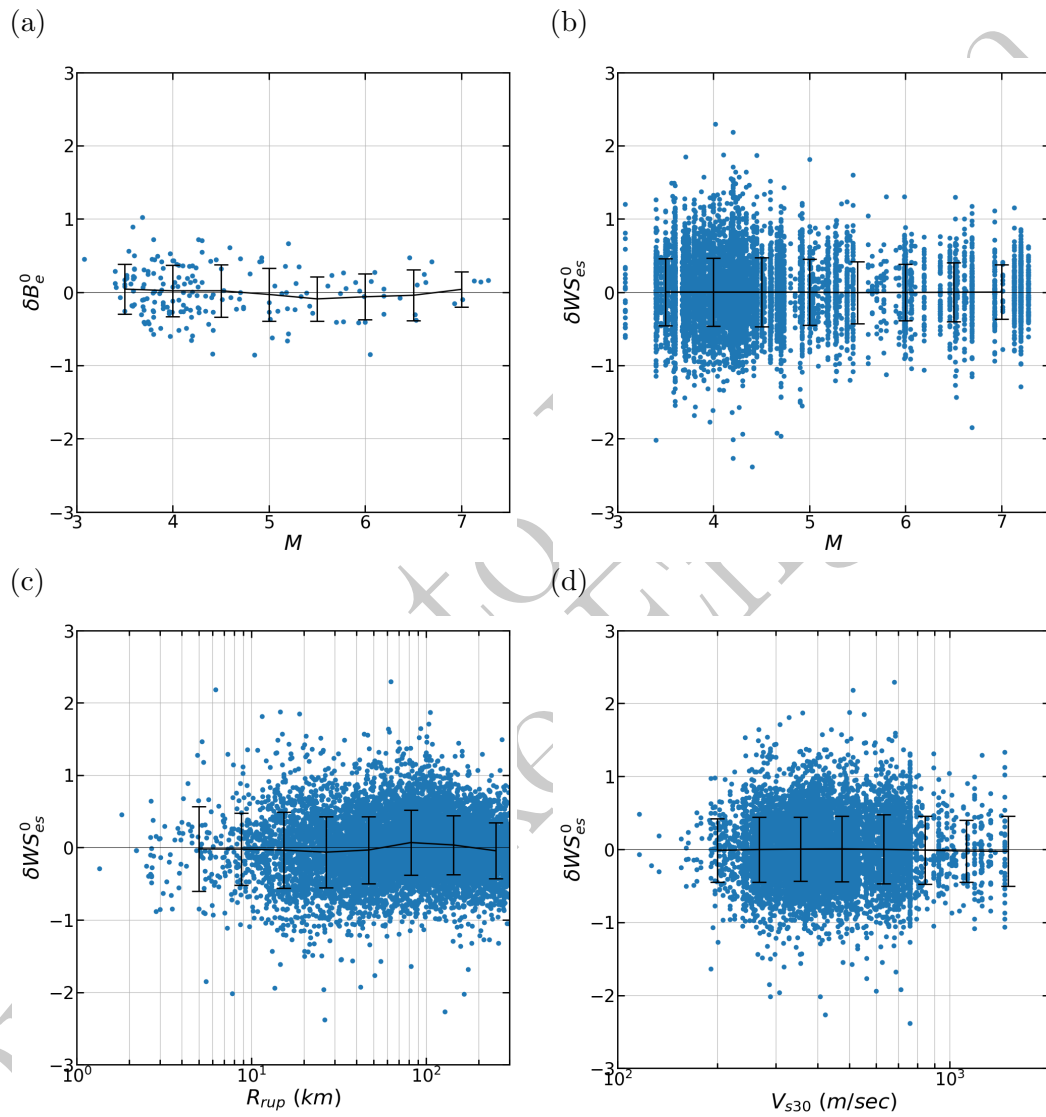


Figure 10: Non-ergodic within-event and between-event residuals at $f = 5Hz$. (a) δB_e^0 versus magnitude, (b) δWS_{es}^0 versus magnitude, (c) δWS_{es}^0 versus rupture distance, and (d) δWS_{es}^0 versus V_{s30} .

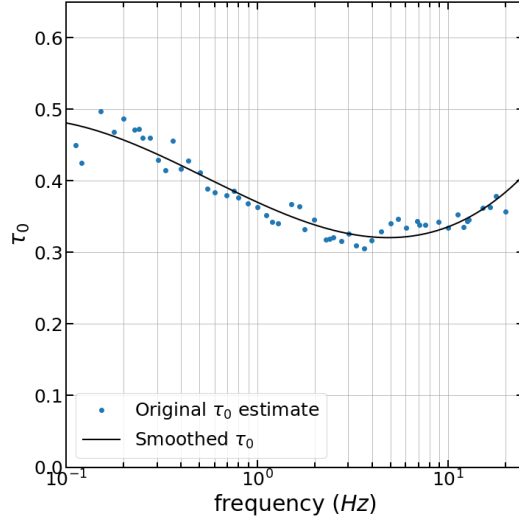


Figure 11: Between-event standard deviation, τ_0 , versus frequency; circular markers correspond to the estimated τ_0 at every frequency, solid line corresponds to smoothed τ_0 .

resulting *EAS* will have a reasonable shape (Figures 11 and 12). The smoothing was performed by fitting the aleatory parameters with a fourth order polynomial. The value of τ_0 decreases from small to intermediate frequencies and increases again after $f = 3\text{Hz}$, which is consistent with the behaviour of BA18 and other *PSA* GMM, such as Abrahamson et al. (2014). The magnitude dependence of ϕ_0 is more pronounced at high frequencies. The higher ϕ_0 of small events at high frequencies is believed to be due to an increased effect of the radiation patterns. At large events, the effect of radiation patterns is smaller as seismic rays originate from more locations along the fault, which increases the range of azimuthal angles, and leads to destructive interference of the radiation patterns resulting in less ground-motion variability. Figure 13 compares the magnitude relationships for τ_0 and ϕ_0 with the empirical standard deviations at $f = 5\text{Hz}$. Overall, there is a good fit between the τ_0 and ϕ_0 relationships and the standard deviations of the binned residuals. The differences at large magnitudes should be reevaluated with a dataset which includes a greater number of large magnitude events.

$$\phi_0 = \begin{cases} \phi_{0M_1} & \text{for } M < 5 \\ \phi_{0M_1} + (\phi_{0M_2} - \phi_{0M_1})(M - 5)/(6.5 - 5) & \text{for } 5 < M < 6.5 \\ \phi_{0M_2} & \text{for } M > 6.5 \end{cases} \quad (36)$$

As a comparison with ergodic aleatory variability, figure 14 shows the total aleatory variability for the non-ergodic GMM for the small and large magnitudes events and the standard deviation of the ergodic residuals used for the derivation of this model. Based on this range, the total aleatory standard deviation of the non-ergodic GMM ranges from 0.50 to 0.65 which is about a 40 to 30% reduction from the standard deviation of the ergodic GMM.

4.5 Inter-frequency correlation

The inter-frequency correlation of the non-ergodic terms is presented in Figure 15 and the model parameters are summarized in Table 4. Currently, the correlation of all non-ergodic terms is modeled as frequency independent: that is, the width of the *EAS* peaks and troughs does not depend their central frequency. A frequency independent correlation would mean that the width of

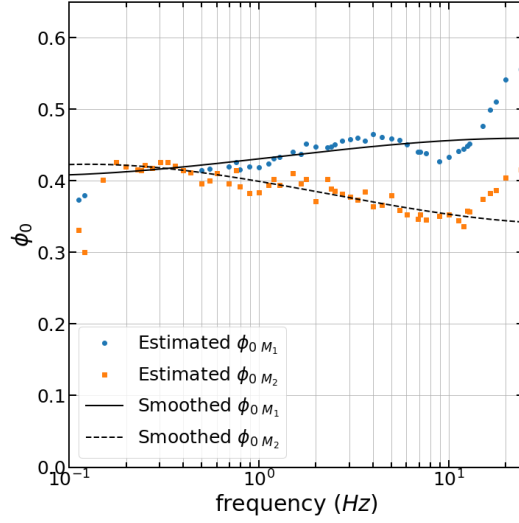


Figure 12: Within-event standard deviation, ϕ_0 , versus frequency; circular markers correspond to the estimated ϕ_0 at small magnitudes, square markers correspond to the estimated ϕ_0 at large magnitudes, solid line corresponds to smoothed ϕ_0 for small magnitudes, dashed line corresponds to the smoothed ϕ_0 for large magnitudes.

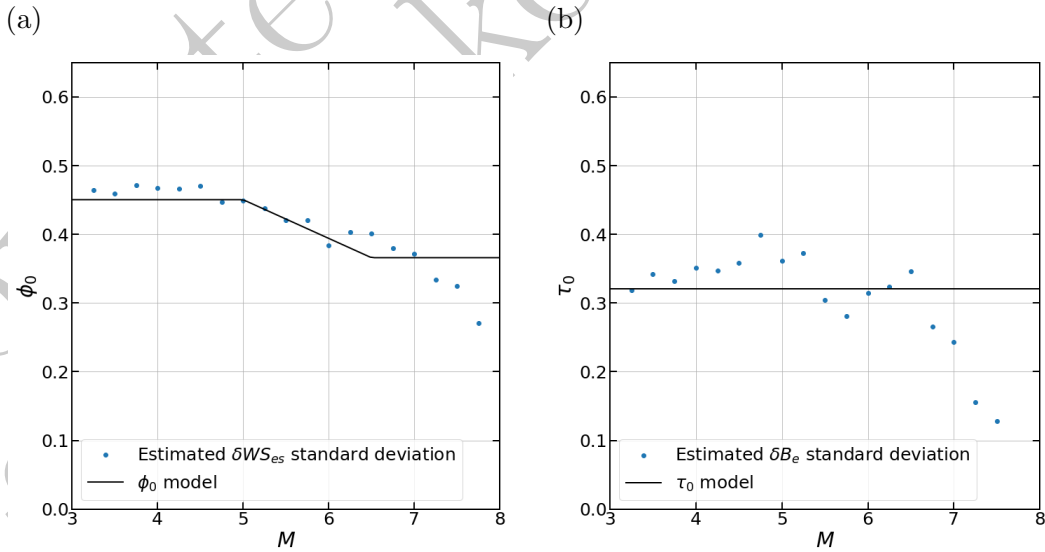


Figure 13: Magnitude scaling of τ_0 and ϕ_0 for $f = 5Hz$; circular markers denote the standard deviations of the binned residuals, and solid lines correspond to the standard deviation models.

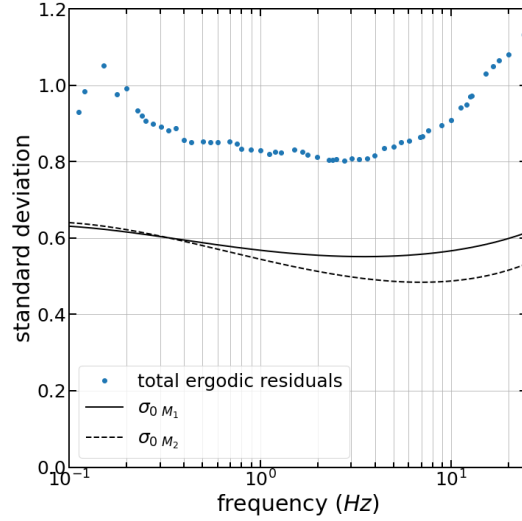


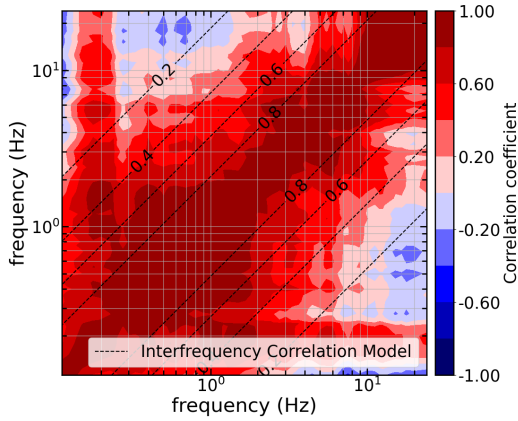
Figure 14: Comparison of total non-ergodic standard deviation with standard deviations of the total ergodic residuals

Table 4: Interfrequency model coefficients for non-ergodic terms

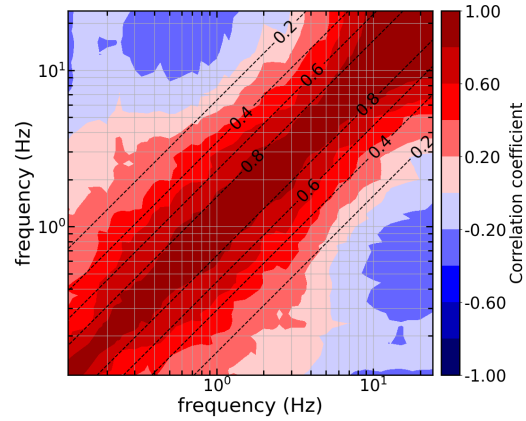
	A	B	C	D
$\delta c_{1,e}$	1.94	0.77	0.96	19.49
$\delta c_{1a,s}$	1.30	0.92	1.36	30.85
$\delta c_{1b,s}$	1.83	1.86	2.77	63.96
$c_{ca,p}$	1.85	0.41	0.27	10.00

the correlation ridges in Figure 15 does not change along the diagonal, whereas a non-constant width would mean that the correlation changes with frequency. Out of all the non-ergodic terms, $\delta c_{1,e}$ has the widest confidence intervals because the number of unique earthquakes is smaller than both the number of unique stations or the number of anelastic attenuation cells. $\delta c_{1,e}$ has a relatively wide correlation, meaning that if $\delta c_{1,e}$ is positive at one frequency, it is highly likely that it will also be positive over a wide range of neighbouring frequencies. The correlation of this term also exhibits some frequency dependence similar to the δB_e frequency dependence found in Bayless and Abrahamson (2019a): the correlation is the widest at $f = 0.5Hz$, it narrows at intermediate frequencies, and it widens again at frequencies larger than $8Hz$. Both $\delta c_{1a,s}$ and $\delta c_{1b,s}$ have narrow, mostly frequency independent, inter-frequency correlations, which are similar to the correlation structure of $\delta S2S$ in Bayless and Abrahamson (2019a). The correlation of $c_{ca,p}$ shows the strongest frequency dependence; there is very little correlation at frequencies less than $1Hz$, it gradually increases and reaches the widest point at $5Hz$, and then, it narrows again. The narrow frequency correlation at low frequencies is expected as the anelastic attenuation is very weak for that frequency range; however, it is unclear why the inter-frequency correlation narrows at high frequencies. It could be an artifact of poor sampling. For now, it is modeled as frequency independent, but in future studies, this assumption would need to be reevaluated. As a point of comparison, in seismic numerical simulations, a deterministic velocity model would imply a perfect inter-frequency correlation on $c_{ca,p}$, which is more similar to the width of the correlation of data at $f = 5Hz$

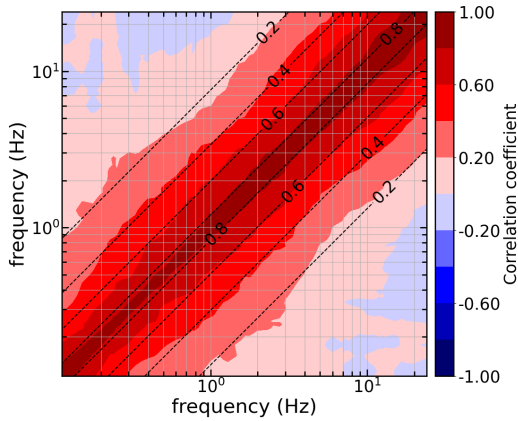
(a)



(b)



(c)



(d)

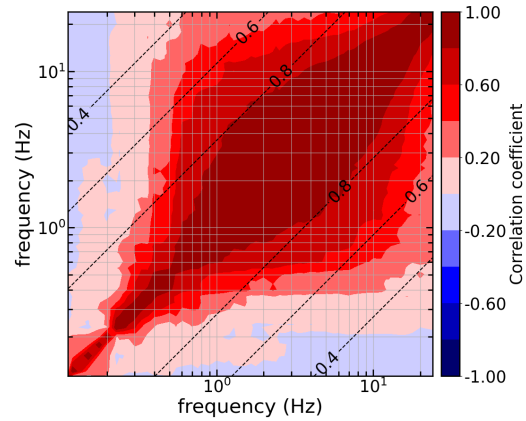


Figure 15: Inter-frequency correlation of non-ergodic terms; contour plot corresponds to the inter-frequency correlation of the data, dashed lines corresponds to the inter-frequency correlation model. (a) inter-frequency correlation of $\delta c_{1,e}$, (b) inter-frequency correlation of $\delta c_{1a,s}$, (c) inter-frequency correlation of $\delta c_{1b,s}$, and (d) inter-frequency correlation of $c_{ca,p}$.

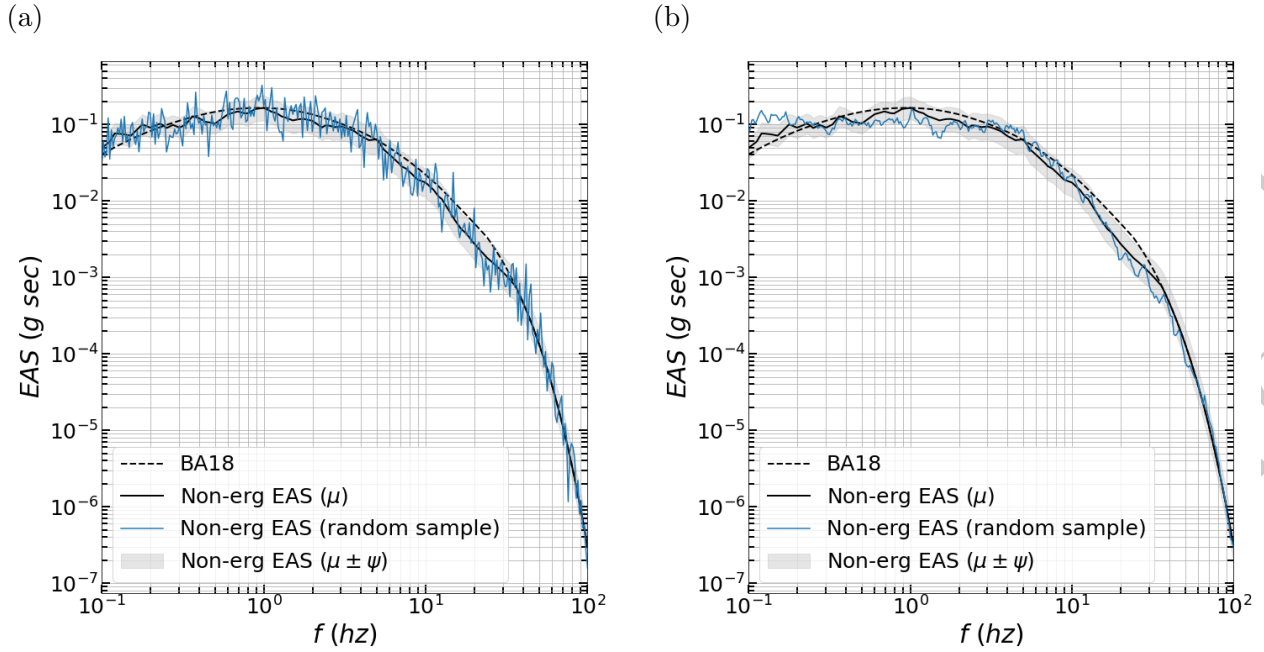


Figure 16: Effective amplitude spectra for a M 7 earthquake, 10 km away for a site located in Berkeley, CA. (a) without inter-frequency correlation, and (b) with inter-frequency correlation.

4.6 Examples

Figure 16 shows the effect of inter-frequency correlation in sampling the non-ergodic terms for an M 7 earthquake in Hayward fault 10 km from a site in Berkeley, CA. Figure 16a shows the median non-ergodic EAS , the 16th to 84th percentile range of epistemic uncertainty, and a representative EAS sample with epistemic uncertainty for zero inter-frequency correlation. Figure 16b shows the same information, but in this case, the ground motions were generated with the inter-frequency correlation model described previously. The median EAS and range of epistemic uncertainty is the same in both cases; what is different are the representative EAS samples. The EAS sample with zero inter-frequency correlation has zero width in the peaks and the troughs, whereas EAS sample with inter-frequency correlation has peaks and troughs that span approximately a quarter of a decade. It should be noted that these samples do not include aleatory variability, the inter-frequency correlation of the aleatory variability will influence the final width of the peaks and troughs.

The distance scaling of the model for $f = 5Hz$ for a site in San Jose, CA (SJ) and a site in Northeastern California (NE) is presented in Figure 17; the site in SJ has a station which has recorded ground motions from past earthquakes to constrain $\delta c_{1b,s}$, whereas the site in NE does not have one, so $\delta c_{1b,s}$ is unconstrained. In both cases, the earthquakes are located north of sites. North of SJ , $c_{ca,p}$ is less than average (Figure 7a) which causes the non-ergodic GMM to have higher attenuation than BA18. Due to the small number of paths in NE , $c_{ca,p}$ is very close to the mean value which is why the non-ergodic GMM and BA18 have similar distance scaling. The epistemic uncertainty is less in SJ as there are more earthquakes and stations to constrain the non-ergodic terms.

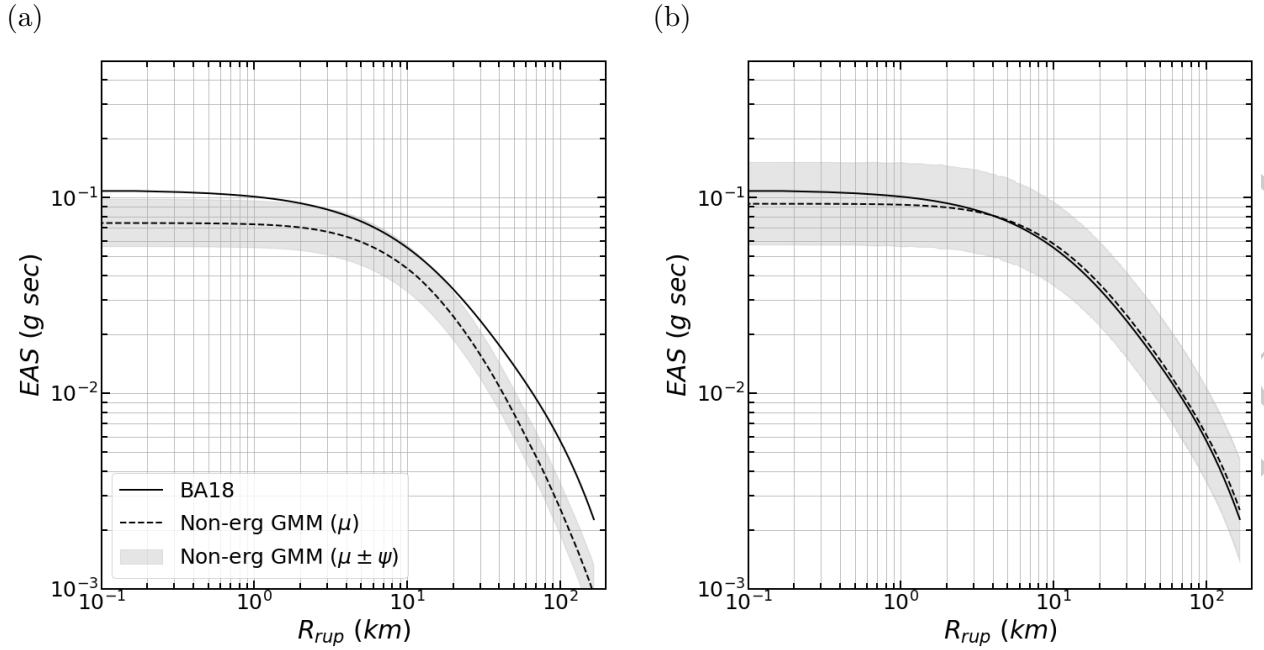


Figure 17: Distance scaling of $EAS(f = 5Hz)$ for (a) a site in San Jose, CA and (b) a site in northeastern California.

5 Model Validation

The performance of the non-ergodic GMM was evaluated with a 5-fold cross validation test using the ground-motion data from $f = 5Hz$. In each of the 5 iterations of the cross-validation test, the NGAWest2 CA dataset was randomly split into a training and test datasets, 80% of the earthquakes composed training dataset and the remaining 20% of earthquakes composed the test dataset. The training set was used to estimate the coefficients of the non-ergodic model, and the test dataset was used to evaluate the accuracy of the predictions with the estimated coefficients. The NGAWest2 CA dataset was split based on the earthquakes so that the non-ergodic GMM is evaluated on events that were not used in the parameter estimation. Figure 18 shows the root-mean-square error ($rmse$) of the non-ergodic GMM and BA18 for all iterations. The average $rmse$ of the non-ergodic GMM and BA18 is 0.66 and 0.87, respectively, which indicates that incorporating the non-ergodic terms improves the ground-motion prediction for events that were not part of the regression dataset.

6 Conclusions and Discussion

A fully non-ergodic EAS GMM is presented in this study. The non-ergodic source and station effects are captured by spatially varying coefficients; the non-ergodic path effects are captured with the cell-specific anelastic attenuation. A regional term that accounts for the differences in the ground motion of small earthquakes between northern and southern California is also added in the non-ergodic GMM; this term is applied to events less than M 5, and frequencies less than $5 Hz$. The exact cause of these differences could not be identified, but it could be related to a potential bias in the magnitude estimation between the NCSN and SCSN networks. Future studies should further investigate the cause of these differences.

The proposed non-ergodic GMM has a 30 to 40% smaller total aleatory standard deviation

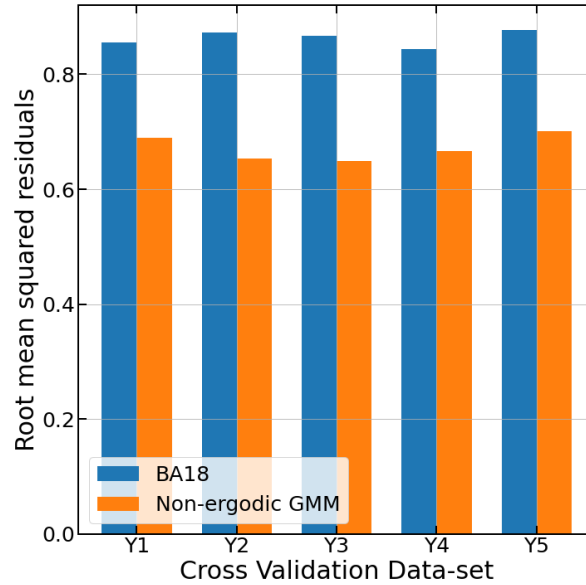


Figure 18: Root-mean-square error of 5-fold cross-validation test

than BA18. Furthermore, the cross-validation test shows that the non-ergodic GMM performs better than BA18 in predicting the ground motion for events that were not part of the regression dataset.

The next step is to use this non-ergodic *EAS* GMM with RVT to develop an equivalent non-ergodic *PSA* GMM. The advantage of this approach is that it is easier to transfer the estimated non-ergodic terms, which are primarily based on small magnitude events, to the non-ergodic terms for the scenarios of interest, which typically are large magnitude events, using RVT than it is to estimate the magnitude dependence during the development of the non-ergodic *EAS* GMM. For the scenarios of interest, the *PSA* non-ergodic terms can be estimated by combining the *EAS* predictions, for the same scenarios, with RVT. In this approach, the magnitude dependence of the non-ergodic *PSA* terms is captured.

As larger data sets become available, future studies should consider the addition of a spatially varying term for geometrical spreading and test the frequency dependence of the inter-frequency correlation of the non-ergodic terms. A spatially-varying geometrical-spreading coefficient may be able to better capture the non-ergodic path effects at short distances; however, if such a coefficient is added, it should be constrained so that the GMM does not over-saturate at short distances. Currently, the inter-frequency correlation of the non-ergodic terms was assumed to be frequency independent, future studies should reevaluate if this assumption is valid.

Currently, the path for the cell-specific anelastic attenuation connects the site with closest point on the rupture. This path was chosen because it is the same path that is used in the R_{rup} calculation; however, it has not been tested whether a path connecting the site and a different point on the rupture would be more appropriate for the cell-specific anelastic attenuation. A large number of broadband earthquake simulations that include 3D velocity structure effects up to high frequencies (e.g. 5 Hz) would be ideal for solving this problem.

7 Acknowledgements

This work was partially supported by the PG&E Geosciences Department Long-Term Seismic Program. The authors also thankful to the three anonymous reviewers for constructive comments that helped to improve the final article.

Declarations

Funding

This work was partially funded by the PG&E Geosciences Department Long-Term Seismic Program.

Conflict of interest

The authors declare that they have no conflict of interest.

Ethics approval

Non applicable

Consent to participate

Non applicable

Consent for publication

Non applicable

Availability of data and material

Code availability

The are python scripts for the non-ergodic regressions are provided at:
https://github.com/glavrentiadis/NonErgodicGMM_public

References

- Abrahamson, N. A., G. M. Atkinson, D. M. Boore, Y. Bozorgnia, K. W. Campbell, B. S. Chiou, I. M. Idriss, W. J. Silva, and R. R. Youngs (2008). Comparisons of the NGA ground-motion relations. *Earthquake Spectra* 24(1), 45–66.
- Abrahamson, N. A., N. M. Kuehn, M. Walling, and N. Landwehr (2019, 7). Probabilistic Seismic Hazard Analysis in California Using Nonergodic Ground Motion Models. *Bulletin of the Seismological Society of America* 109(4), 1235–1249.
- Abrahamson, N. A., W. J. Silva, and R. Kamai (2014). Summary of the ASK14 ground motion relation for active crustal regions. *Earthquake Spectra* 30(3), 1025–1055.

- Akkar, S. and Z. Çağnan (2010). A local ground-motion predictive model for Turkey, and its comparison with other regional and global ground-motion models. *Bulletin of the Seismological Society of America* 100(6), 2978–2995.
- Al Atik, L., N. A. Abrahamson, J. J. Bommer, F. Scherbaum, F. Cotton, and N. M. Kuehn (2010). The Variability of Ground-Motion Prediction Models and Its Components. *Seismological Research Letters* 81(5), 794–801.
- Ancheta, T. D., R. B. Darragh, J. P. Stewart, E. Seyhan, W. J. Silva, B. S. Chiou, K. E. Wooddell, R. W. Graves, A. R. Kottke, D. M. Boore, T. Kishida, and J. L. Donahue (2013). PEER NGA-West2 database. Technical report, PEER, Berkeley, CA.
- Ancheta, T. D., R. B. Darragh, J. P. Stewart, E. Seyhan, W. J. Silva, B. S. Chiou, K. E. Wooddell, R. W. Graves, A. R. Kottke, D. M. Boore, T. Kishida, and J. L. Donahue (2014). NGA-West2 database. *Earthquake Spectra* 30(3), 989–1005.
- Anderson, J. G. and J. N. Brune (1999). Probabilistic seismic hazard analysis without the ergodic assumption. *Seismological Research Letters* 70(1), 19–28.
- Bayless, J. and N. A. Abrahamson (2018). Evaluation of the interperiod correlation of ground-motion simulations. *Bulletin of the Seismological Society of America* 108(6), 3413–3430.
- Bayless, J. and N. A. Abrahamson (2019a). An Empirical Model for the Interfrequency Correlation of Epsilon for Fourier Amplitude Spectra. *Bulletin of the Seismological Society of America* 109(3), 1058–1070.
- Bayless, J. and N. A. Abrahamson (2019b, 10). Summary of the BA18 Ground-Motion Model for Fourier Amplitude Spectra for Crustal Earthquakes in California. *Bulletin of the Seismological Society of America* 109(5), 2088–2105.
- Bindi, D., F. Pacor, L. Luzi, R. Puglia, M. Massa, G. Ameri, and R. Paolucci (2011). Ground motion prediction equations derived from the Italian strong motion database. *Bulletin of Earthquake Engineering* 9(6), 1899–1920.
- Bishop, C. M. (2006). *Pattern Recognition and Machine Learning*. New York, NY: Springer.
- Bommer, J. J., K. J. Coppersmith, R. T. Coppersmith, K. L. Hanson, A. Mangongolo, J. Neveling, E. M. Rathje, A. Rodriguez-Marek, F. Scherbaum, R. Shelembe, P. J. Stafford, and F. O. Strasser (2015). A SSHAC level 3 probabilistic seismic hazard analysis for a new-build nuclear site in South Africa. *Earthquake Spectra* 31(2), 661–698.
- Boore, D. M. (1983). Stochastic simulation of high-frequency ground motions based on seismological models of the radiated spectra. *Bulletin of the Seismological Society of America* 73(6), 1865–1894.
- Bora, S. S., F. Cotton, and F. Scherbaum (2019). NGA-West2 empirical fourier and duration models to generate adjustable response spectra. *Earthquake Spectra* 55(1), 61–93.
- Bora, S. S., F. Scherbaum, N. M. Kuehn, P. J. Stafford, and B. Edwards (2015). Development of a response spectral ground-motion prediction equation (GMPE) for seismic-hazard analysis from empirical fourier spectral and duration models. *Bulletin of the Seismological Society of America* 105(4), 2192–2218.

- Bozorgnia, Y., N. A. Abrahamson, L. Al Atik, T. D. Ancheta, G. M. Atkinson, J. W. Baker, A. S. Baltay, D. M. Boore, K. W. Campbell, B. S. Chiou, R. Darragh, S. Day, J. Donahue, R. W. Graves, N. Gregor, T. C. Hanks, I. M. Idriss, R. Kamai, T. Kishida, A. R. Kottke, S. A. Mahin, S. Rezaeian, B. Rowshandel, E. Seyhan, S. Shahi, T. Shantz, W. J. Silva, P. Spudich, J. P. Stewart, J. Watson-Lamprey, K. Wooddell, and R. R. Youngs (2014). NGA-West2 research project. *Earthquake Spectra* 30(3), 973–987.
- Bragato, P. L. and D. Slejko (2005). Empirical ground-motion attenuation relations for the eastern Alps in the magnitude range 2.5–6.3. *Bulletin of the Seismological Society of America* 95(1), 252–276.
- Brune, J. N. (1970). Tectonic stress and the spectra of seismic shear waves from earthquakes. *Journal of Geophysical Research* 75(26), 4997–5009.
- Brune, J. N. (1971). Correction to Tectonic stress and the spectra of seismic shear waves from earthquakes. *Journal of Geophysical Research* 76(20), 1971.
- Bussas, M., C. Sawade, N. M. Kuehn, T. Scheffer, and N. Landwehr (2017). Varying-coefficient models for geospatial transfer learning. *Machine Learning* 106(9-10), 1419–1440.
- Chiou, B. S., R. Youngs, N. A. Abrahamson, and K. Addo (2010). Ground-motion attenuation model for small-to-moderate shallow crustal earthquakes in California and its implications on regionalization of ground-motion prediction models. *Earthquake Spectra* 26(4), 907–926.
- Chiou, B. S. and R. R. Youngs (2014, 8). Update of the Chiou and Youngs NGA Model for the Average Horizontal Component of Peak Ground Motion and Response Spectra. *Earthquake Spectra* 30(3), 1117–1153.
- Coppersmith, K., J. Bommer, K. Hanson, J. Unruh, R. Coppersmith, L. Wolf, R. Youngs, A. Rodriguez-Marek, L. Al Atik, G. Toro, et al. (2014). Hanford sitewide probabilistic seismic hazard analysis. *PNNL-23361 Pacific Northwest National Laboratory, Richland Washington* <http://www.hanford.gov/page.cfm/OfficialDocuments/HSPSHA>.
- Danciu, L. and G.-A. Tselentis (2007, 2). Engineering Ground-Motion Parameters Attenuation Relationships for Greece. *Bulletin of the Seismological Society of America* 97(1B), 162–183.
- Dawood, H. M. and A. Rodriguez-Marek (2013). A Method for including path effects in ground-motion prediction equations: An example using the Mw 9.0 Tohoku earthquake aftershocks. *Bulletin of the Seismological Society of America* 103(2 B), 1360–1372.
- Douglas, J., S. Akkar, G. Ameri, P. Y. Bard, D. Bindi, J. J. Bommer, S. S. Bora, F. Cotton, B. Derras, M. Hermkes, N. M. Kuehn, L. Luzi, M. Massa, F. Pacor, C. Riggelsen, M. A. Sandikkaya, F. Scherbaum, P. J. Stafford, and P. Traversa (2014). Comparisons among the five ground-motion models developed using RESORCE for the prediction of response spectral accelerations due to earthquakes in Europe and the Middle East. *Bulletin of Earthquake Engineering* 12(1), 341–358.
- Eberhart-Phillips, D. (2016). Northern California seismic attenuation: 3D Qp and Qs models. *Bulletin of the Seismological Society of America* 106(6), 2558–2573.

- Elzhov, T. V., K. M. Mullen, A.-N. Spiess, and B. Bolker (2016). *minpack.lm: R Interface to the Levenberg-Marquardt Nonlinear Least-Squares Algorithm Found in MINPACK, Plus Support for Bounds*. R package version 1.2-1.
- Goulet, C., A. Kottke, D. Boore, Y. Bozorgnia, J. Hollenback, T. Kishida, A. Der Kiureghian, O. Ktenidou, N. Kuehn, E. Rathje, et al. (2018). Effective amplitude spectrum (eas) as a metric for ground motion modeling using fourier amplitudes. In *2018 Seismology of the Americas Meeting*.
- Hiemer, S., F. Scherbaum, D. Roessler, and N. M. Kuehn (2011, 5). Determination of 0 and Rock Site from Records of the 2008/2009 Earthquake Swarm in Western Bohemia. *Seismological Research Letters* 82(3), 387–393.
- Kuehn, N. M., N. A. Abrahamson, and M. A. Walling (2019). Incorporating Nonergodic Path Effects into the NGA-West2 Ground-Motion Prediction Equations. *Bulletin of the Seismological Society of America* 109(2), 575–585.
- Kuehn, N. M., Y. Bozorgnia, K. W. Campbell, and N. Gregor (2020). Partially Non-Ergodic Ground-Motion Model for Subduction Regions using the NGA-Subduction Database. Technical Report September, PEER.
- Kutner, M. H., C. J. Nachtsheim, J. Neter, W. Li, et al. (2005). *Applied linear statistical models*, Volume 5. McGraw-Hill Irwin New York.
- Landwehr, N., N. M. Kuehn, T. Scheffer, and N. A. Abrahamson (2016). A nonergodic ground-motion model for California with spatially varying coefficients. *Bulletin of the Seismological Society of America* 106(6), 2574–2583.
- Lin, P. S., B. S. Chiou, N. A. Abrahamson, M. Walling, C. T. Lee, and C. T. Cheng (2011). Repeatable source, site, and path effects on the standard deviation for empirical ground-motion prediction models. *Bulletin of the Seismological Society of America* 101(5), 2281–2295.
- Phillips, W. S., K. M. Mayeda, and L. Malagnini (2014). How to Invert Multi-Band, Regional Phase Amplitudes for 2-D Attenuation and Source Parameters: Tests Using the USArray. *Pure and Applied Geophysics* 171(3-5), 469–484.
- R Core Team (2020). *R: A Language and Environment for Statistical Computing*. Vienna, Austria: R Foundation for Statistical Computing.
- Rasmussen, C. E. and C. K. I. Williams (2006). Gaussian processes for machine learning. *The MIT Press, Cambridge, MA, USA* 38, 715–719.
- Simpson, D., H. Rue, A. Riebler, T. G. Martins, and S. H. Sørbye (2017). Penalising model component complexity: A principled, practical approach to constructing priors. *Statistical Science* 32(1), 1–28.
- Stafford, P. J., A. Rodriguez-Marek, B. Edwards, P. P. Kruiver, and J. J. Bommer (2017). Scenario dependence of linear site-effect factors for short-period response spectral ordinates. *Bulletin of the Seismological Society of America* 107(6), 2859–2872.
- Stan Development Team (2019). The Stan Core Library. Version 2.25.0.

Tromans, I. J., G. Aldama-Bustos, J. Douglas, A. Lessi-Cheimariou, S. Hunt, M. Daví, R. M. W. Musson, G. Garrard, F. O. Strasser, and C. Robertson (2019, 1). Probabilistic seismic hazard assessment for a new-build nuclear power plant site in the UK. *Bulletin of Earthquake Engineering* 17(1), 1–36.

Yagoda-Biran, G., J. G. Anderson, H. Miyake, and K. Koketsu (2015). Between-event variance for large repeating earthquakes. *Bulletin of the Seismological Society of America* 105(4), 2023–2040.

Submitted to *Bulletin of Earthquake Engineering*